Geophys. J. Int. (2003) **155,** 753–777

What can GPS data tell us about the dynamics of post-seismic deformation?

Elizabeth H. Hearn

Department of Earth and Ocean Sciences, University of British Columbia, Vancouver, BC, Canada. E-mail: ehearn@eos.ubc.ca

Accepted 2003 April 22. Received 2003 February 23; in original form 2002 September 9

SUMMARY

This paper describes differences in time-varying post-seismic deformation due to after-slip and viscoelastic relaxation following large strike-slip earthquakes, and how these differences may be exploited to characterize the configuration and rheology of aseismically deforming material in the subsurface. The analysis involves two steps. First, near-field, time-dependent post-seismic deformation characteristics of a typical $M_w = 7.4$ strike-slip earthquake is defined based on analysis of GPS data from three recent earthquakes. Secondly, this earthquake is modelled (assuming uniform slip along a rectangular surface), and several classes of after-slip and viscoelastic relaxation models that can reproduce the evolution of early post-seismic displacements with time at a near-field reference point are developed. Postseismic displacements and velocities away from the reference point, where the differences are greatest (and thus most likely to be distinguished with GPS) are compared. I find that displacements from a judiciously designed network of continuous or frequently occupied campaign-mode GPS sites are sufficiently precise to distinguish linear viscoelastic relaxation from after-slip on a vertical surface extending the coseismic rupture. Furthermore, both the thickness and viscosity of a relaxing, linearly viscoelastic layer may be identified. To maximize what post-seismic GPS surveys can tell us, particularly concerning potential relaxation of low-viscosity layers in the crust and/or upper mantle, some GPS sites should be located along strike beyond the rupture tip. Also, far-field GPS sites should be occupied as frequently as sites close to the rupture.

Key words: after-slip, GPS, post-seismic, viscoelastic relaxation.

1 INTRODUCTION

Major earthquakes cause static stress changes within the lithosphere that are large enough to excite observable, transient deformation of the Earth's surface. Space geodetic techniques for measuring surface displacements have advanced to the point where both the spatial and temporal characteristics of this post-seismic deformation can be described in detail. This has provided geodynamic modellers with new, powerful data sets for constraining dynamic models of post-seismic deformation.

Efforts to simulate deformation following recent earthquakes, however, have shown that non-unique models of the subsurface may be consistent with post-seismic surface displacement data sets. For example, both after-slip and relaxation of low-viscosity lower crust have been put forward to explain long-wavelength, rapidly decaying crustal deformation during the first 6 months after the 1992 Landers, California earthquake (Shen *et al.* 1994; Yu *et al.* 1996). Later deformation (6 months to 7 yr after the earthquake) has also been explained with different after-slip and viscoelastic relaxation models (e.g. Savage & Svarc 1997; Deng *et al.* 1998; Freed & Lin 2001; Pollitz *et al.* 2001).

Some of this non-uniqueness arises from calibrating models to different displacement fields, even when GPS data from the same sources are used. Differences can result from using data from different groups of GPS sites; including or neglecting inSAR range changes in the analysis; focusing on different time intervals, or applying different corrections for secular deformation. Another reason for the lack of consensus among Landers post-seismic deformation models is that differences in displacement patterns produced by various processes may be small, relative to GPS measurement errors. Still, resolving the cause of post-seismic deformation is important: after-slip or viscoelastic relaxation of materials distributed in various ways in the crust may stress the crust and upper mantle in significantly different ways while producing comparable surface deformation (Hearn *et al.* 2002).

With the recent funding of the Plate Boundary Observatory (PBO) and the Southern California Earthquake Center (SCEC II), increasingly detailed measurements of surface deformation will be collected following future earthquakes in western North America. In light of this, we need to ask some fundamental questions, namely: (1) can after-slip and viscoelastic relaxation of horizontal layers be distinguished from each other with GPS data, given typically

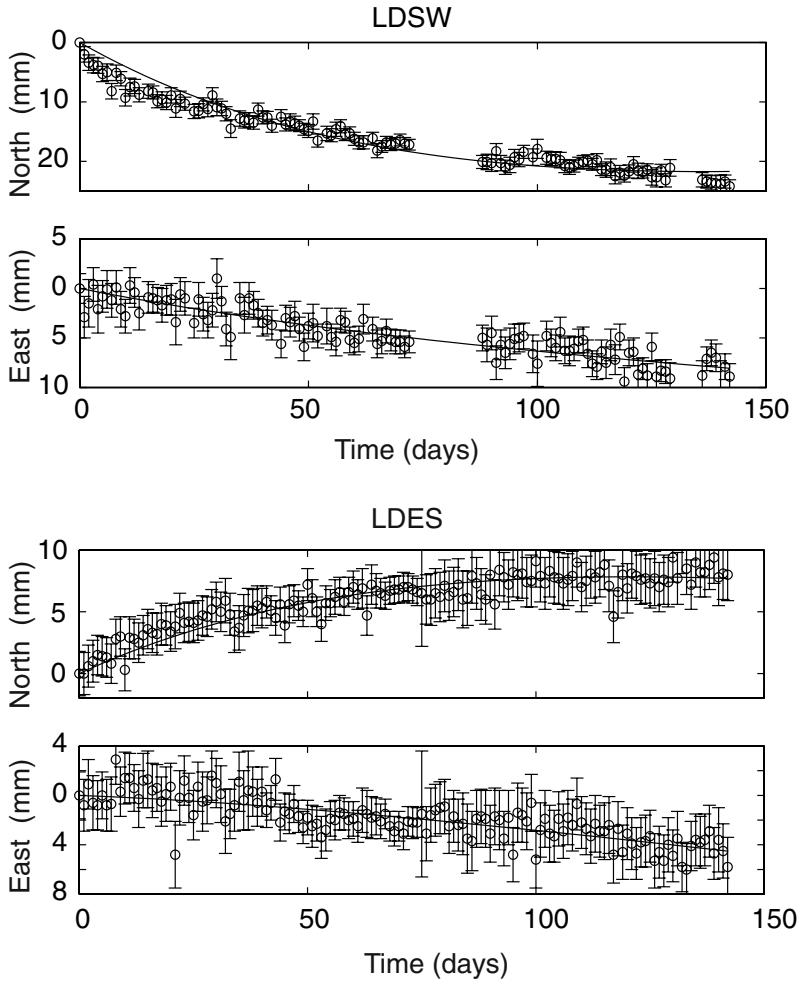

Figure 1. Horizontal displacements as a function of time, from GPS sites near the Hector Mine (LDES and LDSW), Landers (LAZY and PAXU) and Izmit (TUBI and DUMT) earthquake ruptures.

available coverage and measurement precision and if so, (2) how should we monitor post-seismic deformation to maximize the likelihood of differentiating between competing models?

To address these questions, I develop several after-slip and viscoelastic crust or mantle relaxation models that reproduce time-dependent post-seismic displacements typical of recent major strike-slip earthquakes at a near-field reference point. I show that spatial patterns and temporal evolution of post-seismic displacements predicted by these models differ, and point out how they can be distinguished from each other with space geodetic data. I also suggest how GPS networks monitoring post-seismic deformation following large strike-slip earthquakes should be designed to maximize what they can tell us about the structure and rheology of the lithosphere.

2 SURFACE DEFORMATION FROM MAJOR EARTHQUAKES ON STRIKE-SLIP FAULTS

This paper focuses on early post-seismic deformation because it is at this time, when surface velocities and accelerations are highest, that we have the best chance of precisely characterizing the temporal evolution and spatial pattern of this transient deformation. At GPS sites where frequent, high-precision data are available, a decaying transient with a characteristic decay time (τ_c) of 30–80 d can often be identified in at least one horizontal motion component (e.g. Shen *et al.* 1994; Savage & Svarc 1997; Ergintav *et al.* 2002; Owen *et al.* 2002) following large strike-slip earthquakes. This is apparent in the displacement–time curves shown on Fig. 1, and on additional data plots from Shen *et al.* (1994), Savage & Svarc (1997), Ergintav *et al.* (2002) and Owen *et al.* (2002). Similar episodes of transient surface deformation follow subduction zone earthquakes (Webb & Melbourne 1996; Heki *et al.* 1997) and shallow thrust faulting events (Hsu *et al.* 2002). The rapidly decaying transient deformation is superimposed on a more slowly decaying deformation transient (Bock *et al.* 1997; Savage & Svarc 1997), which may contain some contribution from the $\tau_c = 20$–100 yr decaying deformation mode identified from post-1906 San Andreas earthquake strain data (Thatcher 1983; Kenner & Segall 2000).

Since the first part of this study involves developing models that produce near-field post-seismic deformation typical of a $M_w = 7.4$ strike-slip earthquake, a reference point for comparisons between modelled and 'typical' (observed) post-seismic displacements must be chosen. For the earthquake model described below, I define a point located on a perpendicular line bisecting a hypothetical, rectangular earthquake rupture and at a distance of 15 km from the rupture as the reference point, 'Station A' (Fig. 2). For a planar rupture with uniform slip, azimuths at this location will not vary over time and no

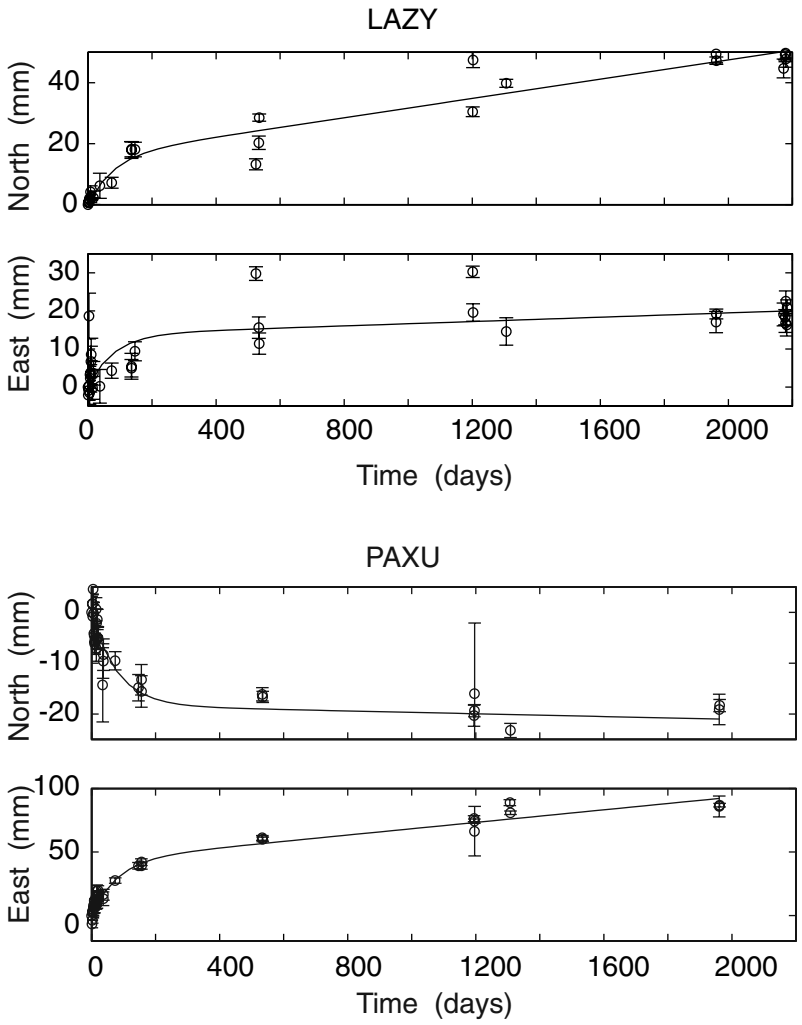

Figure 1. (*Continued.*)

vertical motion will occur, so comparing model results to the Station A displacement–time curve is less complicated than it would be if Station A were in another location. Another reason for choosing this near-field location as a reference point is that post-seismic GPS surveys have historically concentrated on sites close to the earthquake rupture, so more GPS data are available in this area. The next section describes how a 'typical' post-seismic displacement–time curve for Station A was inferred from GPS observations following three recent earthquakes.

2.1 Individual earthquakes

'Typical' post-seismic displacements at reference Station A within 1 yr of a $M_w = 7.4$ strike-slip earthquake are based on an analysis of GPS data from the 1999 Izmit, Turkey; 1999 Hector Mine, California; and 1992 Landers, California earthquakes. In the following sections, I describe post-seismic surface deformation following each of these earthquakes, and then discuss how these data were used to arrive at the station a displacement–time curve.

2.1.1 1992 Landers, California earthquake

The SCEC and the USGS GPS networks in southern California (e.g. Shen *et al.* 1994; Savage & Svarc 1997) provide 7 years of measurements of post-seismic deformation triggered by the 1992 Landers earthquake (i.e. up to the time of the 1999 Hector Mine earthquake). These data have been combined, placed in a stable North America reference frame, and reprocessed together using the GAMIT and GLOBK GPS data processing packages. The post-seismic displacement–time data were corrected for contributions from secular deformation, which were estimated using an elastic block model (Souter 1998; McClusky *et al.* 2001). The east and north displacement components (E_t and N_t) were then fitted to functions with exponential and linear components:

$$E_t = E_{\exp}\left(1 - \mathrm{e}^{-t/\tau}\right) + E_{\mathrm{lin}}\left(\frac{t}{365}\right) \quad (1)$$

$$N_t = N_{\exp}\left(1 - \mathrm{e}^{-t/\tau}\right) + N_{\mathrm{lin}}\left(\frac{t}{365}\right), \quad (2)$$

where $E_{\exp}$, E_{lin}, $N_{\exp}$ and N_{lin} are amplitudes of the exponential and linear components. Overall, exponential decay times (τ_c) of 80–200 d fit the data best, but the sensitivity of the misfit to τ_c is low for sites that were surveyed infrequently. When I fix τ_c at 80 d (consistent with Savage & Svarc 1997), the normalized rms values fall within the 95 per cent confidence interval of χ^2 for the number of degrees of freedom at each site (i.e. the number of observations). The fit of the data-fitting functions (eqs 1 and 2) to the

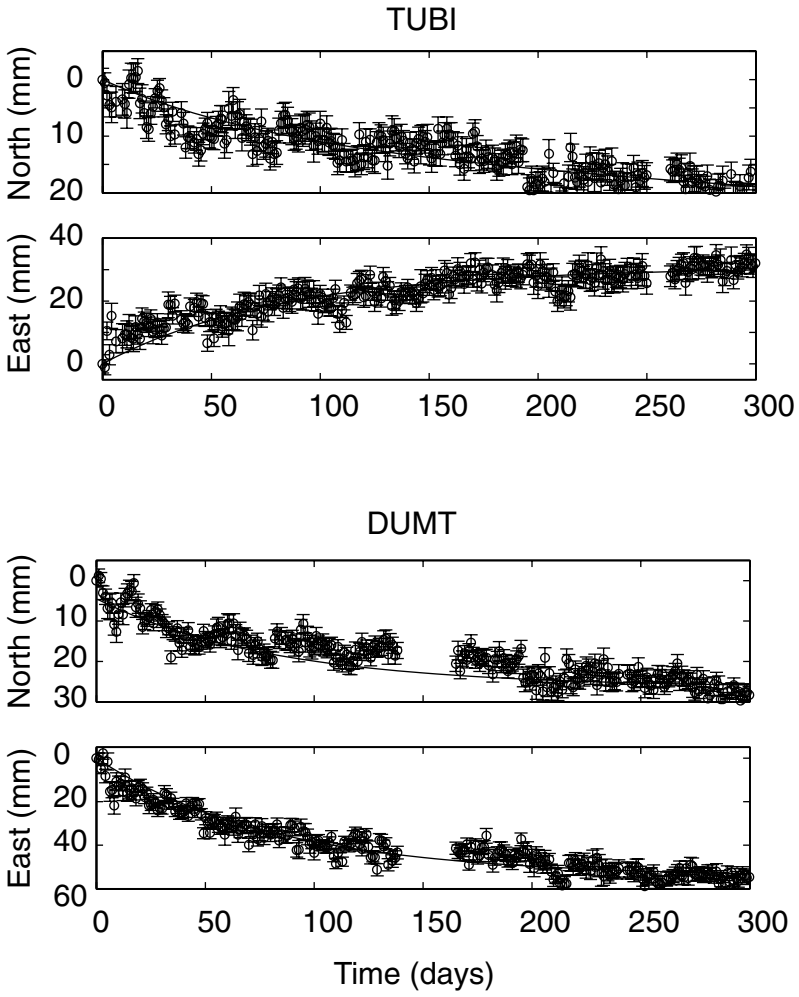

Figure 1. (*Continued.*)

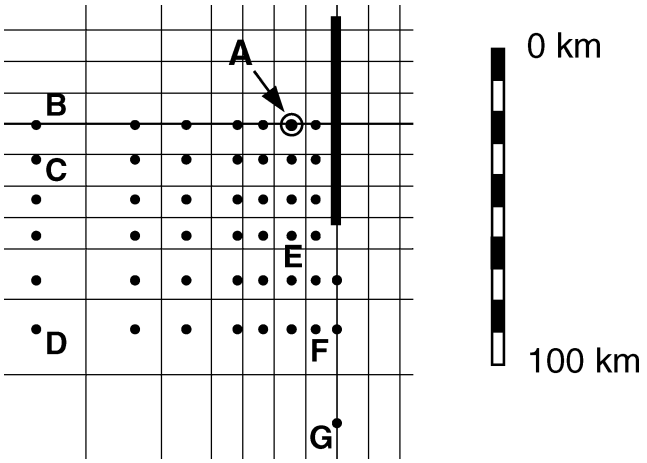

Figure 2. Modelled strike-slip rupture (plan view, one quadrant) and locations of hypothetical GPS stations A–G where displacements are calculated.

east and north displacements is shown for near-field sites LAZY and PAXU in Fig. 1. Although resolution of the decay time is poor for many (less frequently monitored) sites, they clearly require a decaying velocity transient in at least one horizontal direction (usually the north component). At these sites, even where the decay time is not well resolved, errors in the estimated amplitude of the decaying transient are generally less than 20 per cent. At some sites, the data are insufficient to resolve whether a decaying transient is present or not. In these locations, estimates of τ_c (usually of the order of hundreds of days) are associated with large errors (i.e. a 1σ error equal to the estimated decay time or greater). Fig. 3 shows the amplitudes of the exponential and linear terms comprising the displacement–time curve that best fits the horizontal GPS displacement magnitudes (A_t) at each site, plotted against distance from the rupture. The amplitudes of these terms ($\bar{A}_{\rm exp}$ and $\bar{A}_{\rm lin}$) are normalized to the horizontal, coseismic site displacement (A_c). At sites where coseismic displacements were unavailable (for all three earthquakes), A_c was estimated using an elastic dislocation model. The equation for horizontal post-seismic displacement at each GPS site is

$$A_t = A_c \left[\bar{A}_{\rm exp} \left(1 - e^{-t/\tau}\right) + \bar{A}_{\rm lin} \left(\frac{t}{365}\right) \right]. \quad (3)$$

I should note here that the early post-seismic velocities are described as decaying exponentially with time simply because it is convenient. Describing the displacement–time curves with exponential functions is not meant to imply that viscoelastic relaxation is the cause rather than after-slip (which can produce logarithmic velocity decay in the near field; Marone *et al.* 1991). Furthermore,

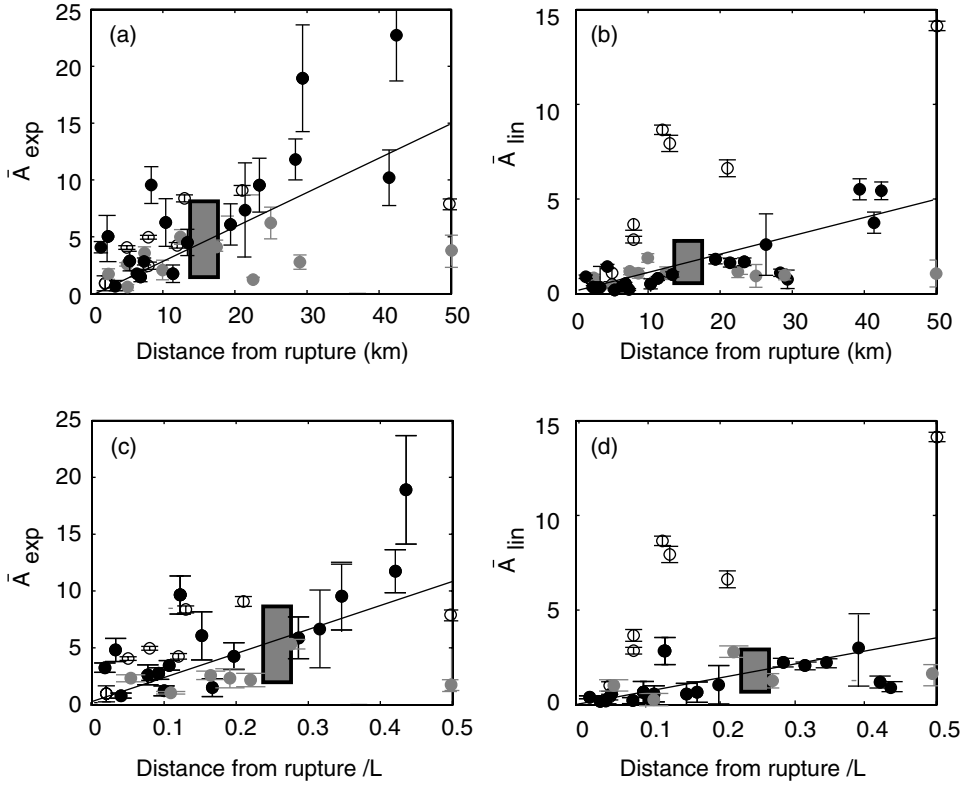

Figure 3. $\bar{A}_{\rm exp}$ and $\bar{A}_{\rm lin}$ for individual GPS sites following the Hector Mine, Landers and Izmit earthquakes. Black, grey and open circles represent data from the Landers, Hector Mine and Izmit earthquakes, respectively. Top (a and b): $\bar{A}_{\rm exp}$ and $\bar{A}_{\rm lin}$ plotted against distance from the rupture. Bottom (c and d): $\bar{A}_{\rm exp}$ and $\bar{A}_{\rm lin}$ plotted against normalized distance to the fault (i.e. distance/rupture length L). Available data for the Izmit and Hector Mine events covered shorter time intervals (300 and 140 d, respectively) than data from the Landers earthquake (2200 d), leading to larger errors in the estimates of $\bar{A}_{\rm exp}$ and $\bar{A}_{\rm lin}$. Thus, only data from continuous GPS sites are shown for the former two earthquakes.

analytical solutions for 2-D models of a dislocation in an elastic layer over a viscoelastic half-space represent the evolution of surface displacements with time as an infinite sum of exponentials with different decay times and amplitudes (e.g. Nur & Mavko 1974; Rice 1980; Pollitz 1997; Cohen 1999). Only at sites very close to the fault does a single exponential term dominate.

2.1.2 1999 Hector Mine, California and Izmit, Turkey earthquakes

Post-seismic displacement data from the first 6 months following the Hector Mine earthquake were processed and fitted to the data-fitting function (eq. 3) as described above for the Landers earthquake. As with the Landers data, horizontal displacement components from some sites showed decaying velocities that could be fitted with eqs (1) and (2) (e.g. sites LDES and LDSW in Fig. 1). Data from sites that were not frequently occupied, or that were far from the rupture, are fitted equally well without an exponential term. Decay times of 20–80 d were preferred by displacement data where an exponential term was required. When I fix $\tau_{\rm c}$ at all sites to 40 d, the nrms values fall within the 95 per cent confidence interval of χ^2 for the number of degrees of freedom at each site (i.e. the number of observations). Resolution of the decay time is poor at most of the campaign-mode GPS sites, but errors in the estimated amplitude of the decaying transient are generally less than 20 per cent. For each site, $\bar{A}_{\rm exp}$ and $\bar{A}_{\rm lin}$ are plotted against distance to the rupture in Fig. 3. Post-seismic displacements for the first 300 d following the Izmit earthquake have also been fit with summed exponential and linear functions (Ergintav *et al.* 2002) and $\tau_{\rm c}$ is about 60 d. Before the analysis was done, the GPS data were corrected for displacements associated with the nearby Düzce earthquake, which occurred 87 d after the Izmit earthquake. The data from Ergintav *et al.* (2002) were also corrected for secular velocities using velocities from a block model (Meade *et al.* 2002) and, where available, pre-Izmit velocity data (McClusky *et al.* 2000). The fit of eqs (1) and (2) to the east and north displacements is shown for near-field sites TUBI and DUMT in Fig. 1. For each GPS site, $\bar{A}_{\rm exp}$ and $\bar{A}_{\rm lin}$ are plotted against distance to the rupture in Fig. 3.

2.2 Synthetic, near-field post-seismic displacements versus time

For each earthquake, representative values of $\bar{A}_{\rm exp}$ and $\bar{A}_{\rm lin}$ at Station A were estimated by least-squares fitting a line to plots of these parameters against distance from the rupture (Fig. 3) and interpolating their magnitudes at $0.25L$. In absolute length, $0.25L$ is 11, 16 and 25 km for the Hector Mine, Landers and Izmit earthquakes. Fig. 3 shows the magnitude of $\bar{A}_{\rm exp}$ and $\bar{A}_{\rm lin}$ for sites within half a rupture length (i.e. $0.5L$) of each fault, plotted against the distance between the site and the rupture. For each earthquake, magnitudes of the exponential and linear (velocity) terms correlate with distance to the fault: correlation coefficients range from 0.61 to 0.76. For the Landers earthquake, the exponential term magnitude was 5 per cent of the coseismic displacement, and the velocity term was 1.5 per cent of the coseismic displacement per year. Similar results are obtained from the Hector Mine earthquake data. Data from the $M_w = 7.5$ Izmit earthquake seem to require a larger $\bar{A}_{\rm exp}$, but the

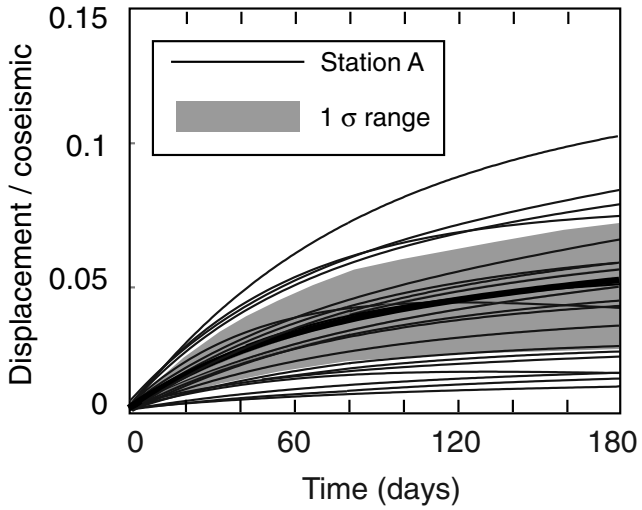

Figure 4. Curve fit to displacement–time data from GPS sites within a distance of $L/2$ of each of the three earthquake ruptures. The hypothetical Station A displacement–time curve is superimposed (heavy black line). The shaded area brackets the plus or minus 50 per cent interval for the Station A displacement–time curve.

displacement–time data at many of the sites do not cover a long enough time interval to properly separate the ($\tau_c \geq 80$ d) exponential term from the linear term.

Since the longest-duration post-seismic displacement data set is from the Landers earthquake, I model an earthquake of comparable magnitude ($M_w = 7.4$) and use the Landers data to define $\bar{A}_{\rm lin}$. $\bar{A}_{\rm exp}$ for Station A is an average of its values for the three earthquakes, which is equal to its value for the Landers earthquake alone. The modelled coseismic displacement at Station A due to the reference $M_w = 7.4$ strike-slip earthquake (described below) is 0.52 m, so the amplitude of the decaying transient and the long-term velocity are 26 and 8 mm yr^{-1}, respectively. Fig. 4 shows the Station A displacement versus time curve, together with displacement versus time curves for GPS sites located within half a rupture length of each earthquake. The Station A curve appears to be representative of near-field, post-seismic deformation following all three earthquakes: at any given time, displacements at most of these GPS sites are within 50 per cent of the Station A displacement.

2.3 'Typical' data errors

Since one point of this project is to evaluate whether differences in surface displacements produced by various post-seismic processes can be discerned with GPS data, 'reasonable' errors associated with these measurements must be defined. The precision of campaign-mode GPS measurements of post-seismic displacements is highly variable, and depends on the frequency and duration of occupations, how soon after the earthquake displacement measurements were made, and on the duration of position monitoring at the site prior to the earthquake (i.e. how well the pre-earthquake velocity of the site was known). GPS sites that were operating prior to an earthquake, and which are monitored frequently (i.e. at least weekly) may measure post-seismic displacements to within a 1σ error (68 per cent confidence interval) of 1 mm (T. Herring, personal communication, 2001). However, GPS networks designed to observe post-seismic deformation often include many sites where pre-earthquake velocities are not known, and frequent monitoring during the first few weeks after an earthquake is often not possible because of logistical challenges. I will assume 1σ errors of 3 and 1 mm, respectively, are possible at campaign-mode and continuous GPS sites, respectively. These are comparable to many of the 1σ errors for post-seismic displacements following the Izmit and Hector Mine earthquakes (e.g. Fig. 1; Ergintav *et al.* 2002; Owen *et al.* 2002), and measurement precision (under optimal circumstances) continues to improve with time. Vertical displacement estimates from GPS are associated with larger errors than horizontal displacement estimates. A typical 1σ measurement error for a Landers earthquake, post-seismic vertical displacement is 10 mm (e.g. Savage & Svarc 1997). Smaller errors (3–5 mm) should be possible at continuous stations (T. Herring, personal communication, 2001) though for the Izmit and Hector Mine earthquakes, most errors in vertical position estimates at continuous GPS sites were considerably larger. InSAR range change measurements may provide vertical displacement estimates if horizontal contributions to range change can be removed. However, even if a perfect correction for horizontal contributions is possible, 1σ errors associated with inSAR vertical displacement estimates should be of the order of a centimetre. Because of difficulties associated with obtaining precise measurements of post-seismic vertical displacements, most of the discussion in the following sections concerns horizontal displacements.

3 MODELLING METHOD

3.1 Viscoelastic finite-element code

I model coseismic and post-seismic deformation using a viscoelastic finite-element code developed specifically for geological applications (Saucier *et al.* 1992; Saucier & Humphreys 1993). This code (GAEA) models 3-D, time-dependent displacements and stresses throughout a volume due to imposed boundary conditions and/or fault slip. Because GAEA incorporates quadratic block elements, curvilinear fault surfaces with smoothly varying slip may be represented. Stresses on these surfaces (which lie along interfaces between elements and are typically interpolated) may also be estimated with a precision greater than that possible for models incorporating linear shape functions and similar nodal spacing.

I have run several elastic and viscoelastic test models to compare the performance of GAEA with that of other programs. Coseismic displacements from a $M_w = 7.4$ strike-slip earthquake (described below) were calculated using GAEA, TEKTON 2.2 (Melosh & Raefsky 1981) and 3D-DEF (Gomberg & Ellis 1994). Elastic surface displacements for GAEA, TEKTON and 3D-DEF are in agreement throughout the modelled region to within about 2 per cent, except within a few kilometres of the fault tip (i.e. within less than one model element dimension) and beyond two fault lengths from the modelled rupture, where amplitudes are less than about 0.5 mm.

For a viscoelastic lower-crust model, I compared post-seismic displacements that were calculated using GAEA, TEKTON 2.2 (Melosh & Raefsky 1981) and VISCO1D (Pollitz 1997). The models produced similar patterns and magnitudes of surface deformation within about 100 km of the fault over 1 year (six Maxwell times). As a result of fixed boundary conditions, GAEA and TEKTON yield more pronounced decay in amplitudes with distance than VISCO1D, but vector azimuths, vertical displacement patterns and time-dependent changes in velocities and azimuths are similar.

To dynamically model after-slip, GAEA calculates shear stresses acting on planes tangent to the fault surface at each fault node,

and calculates slip rates for each time step based on either velocity-strengthening friction or viscous flow laws (described in subsequent sections). Though frictional and viscous properties are specified at each nodal position and may vary spatially, I restrict this study to faults or shear zones with depth-varying properties. To model non-linear viscoelastic relaxation, GAEA calculates deviatoric stress ($\sigma_1 - \sigma_3$) at the centre of each model element and uses this stress to calculate the effective viscosity of the element at the start of each time step.

GAEA inverts for parameters by either a grid search or a Monte Carlo approach, selecting the parameter set that minimizes the squared residual between the posited Station A displacements (Fig. 4) and modelled displacements, summed over 36 10 d intervals (i.e. 1 yr).

Gravitation is not incorporated in these models. For models with linearly viscoelastic layers, gravitation may perturb vertical displacement solutions if $t > 50T_M$ (Pollitz 1997), where T_M, or Maxwell time, is viscosity (η) divided by shear modulus (G). Post-seismic displacements presented in this paper are calculated for $t < 25T_M$.

3.2 Model mesh

The model mesh covers a region of 520 × 520 × 250 km^3, and is centred on a N–S oriented, vertical rupture. The planar rupture is 65 km long and extends from the free surface to a depth of 15 km. 3 m of right-lateral, horizontal slip is imposed along this surface using 'split nodes' (Melosh & Raefsky 1981). The modelled volume is a Poisson solid with a Young's modulus (E) of 70 GPa.

The base and sides of the modelled volume are fixed, and the top surface is unconstrained. To make sure this choice of boundary conditions was reasonable, I evaluated the effect of the fixed basal and side boundaries on coseismic and post-seismic stresses and displacements. Comparing elastic models with stress-free and fixed basal boundaries, I found the difference to horizontal shear stresses resolved on to fault nodes to be less than 5 per cent down to depths of up to 150 km, and effects on surface displacements were negligible. Modelling the side boundaries as fixed or unconstrained, I found that horizontal surface displacements up to 150 km from the rupture trace matched to within about 5 per cent, and that fault zone stresses were nearly identical at all depths. The largest differences in coseismic displacements and fault surface stresses were in the far field and at depth, where their magnitudes were low (less than a millimetre and 0.001 MPa, respectively).

I also evaluated the effect of fixed bottom and side boundary conditions on post-seismic surface displacements and stresses after 1 yr (six Maxwell times), using a viscoelastic lower-crust model. Results from a version of this model with fixed side and bottom boundaries were compared with results from a version with unconstrained boundaries on the bottom and the two sides bounding the quadrant in which stresses and displacements were calculated. Post-seismic surface displacements from the two models differ by less than 2 per cent within 100 km of the rupture. The relative differences in far-field displacements are greater, but both models indicate total post-seismic displacements after 1 yr of less than 0.5 mm (i.e. not detectable with GPS) in these areas.

3.3 Post-seismic deformation models

Each of the models in this paper focuses on a single process, such as after-slip or relaxation of a particular low-viscosity layer. This process is not responsible for all aseismic deformation along a plate boundary throughout the earthquake cycle: to connect the relative motion of two sides of a fault to relatively steady relative plate motions at depth, aseismic processes must occur from the seismogenic zone to the upper mantle. For example, if frictional after-slip is responsible for early post-seismic deformation, a second, slower aseismic process (such as viscoelastic relaxation of the lower crust or a deep extension of the shear zone) must accommodate the relative plate motion between the Moho and the middle crust. The models described below address only the most rapidly occurring aseismic deformation process.

3.3.1 Viscoelastic layers

In models incorporating, viscoelastic layers or the elastic upper crust thickness, H, as well as the viscosity (η) and thickness (h) of the viscoelastic layer, are varied.

For the linear viscoelastic models (groups 1A, 1B and 1C), elastic crust thicknesses (H) of 15, 25 and 33 km, respectively, are modelled (Table 1). Since the base of the rupture is always at 15 km depth, this means the fault penetrates 100, 60 or 45 per cent of the elastic layer. Within each of these groups, four different values of viscoelastic layer thickness (h) and several viscosity values are modelled.

Viscoelastic relaxation of crust or mantle layers with non-linear rheology (group 2A and 2B models) is modelled assuming a stress exponent (n) of 3. I parametrize the non-linear behaviour rather than forward modelling specific flow laws, which would be a less efficient way to match the Station A displacements. Non-linear flow laws for rocks comprising the crust and mantle are generally of the form

$$\eta_{\text{eff}} = \frac{\mu^n}{A\sigma^{n-1}} \exp\left(\frac{E^* + PV^*}{RT}\right). \tag{4}$$

In eq. (4), E^* is the activation energy, P is the pressure, T is the temperature, μ is the shear modulus, V^* is the activation volume, R is the gas constant, A is an empirically determined constant, σ is the differential stress ($\sigma_1 - \sigma_3$) and η_{eff} is the effective viscosity. These parameters vary dramatically with rock type and volatile content, and these are not well constrained for the lower continental crust. Furthermore, eq. (4) requires σ as an input, but absolute values of lower crustal stresses are not known. Rather than guessing reasonable compositions and stresses to calculate η_{eff} directly using eq. (4), my approach is to determine what the parameters in eq. (4) would have to be in order to reproduce near-field, early post-seismic deformation typical of large earthquakes. Since

$$\eta_{\text{eff}}\sigma^{n-1} = \text{constant} \tag{5}$$

non-linear flow laws may be parametrized with a pre-earthquake differential stress (σ_{pre}), a pre-earthquake effective viscosity (η_{pre}), and a stress exponent n (assumed to be 3):

$$\eta_{\text{eff}(t,\text{elem})} = \eta_{\text{pre}}\left[\frac{\sigma_{\text{pre}}}{\sigma_{\text{pre}} + \sigma_{(t,\text{elem})}}\right]^2 \tag{6}$$

where $\eta_{\text{eff}(t,\text{elem})}$ and $\sigma_{(t,\text{elem})}$ are the effective viscosity and the differential stress (coseismic plus post-seismic) in the model element at time t after the earthquake. Since $\sigma_{(t,\text{elem})}$ is calculated by the finite-element code prior to each time step, and $n = 3$, the only free parameters are η_{pre} and σ_{pre}, which are randomly sampled from a wide range of permissible values. The group 2A and 2B models do not take depth variation of η_{pre} and σ_{pre} into account. $\eta_{\text{eff}(t,\text{elem})}$ drops at the time of the earthquake because of the coseismic element

Table 1. Summary of optimal model input parameters, and the misfit to the Station A displacement–time curve. The misfit is reported as WRSS, which is the sum over 36 10 d intervals of the square of the misfit in each horizontal displacement component divided by reasonable measurement errors (2 mm). Note that there is no vertical displacement at Station A because of its location along a nodal surface separating compressional and dilational quadrants (i.e. no poloidal contribution).

Group	H (km)	h (km)	η (Pa s)	T_E (d)	T_M (d)	WRSS (m^2)
Linear viscoelastic models						
1A	15	2	3.2×10^{17}	580	120	0.001
	15	15	1.9×10^{18}	450	740	0.002
	15	30	1.9×10^{18}	380	1000	0.002
	15	125	2.6×10^{18}	80	960	0.002
1B	25	2	4×10^{16}	120	16	0.000 13
	25	8	2×10^{17}	90	61	0.0004
	25	25	4×10^{17}	110	200	0.002
	25	115	6.4×10^{17}	41	250	0.002
1C	33	3	1.3×10^{16}	13	2	0.000 28
	33	17	10^{17}	35	30	0.000 04
	33	52	1.3×10^{17}	30	77	0.000 27
	33	107	1.4×10^{17}	19	100	0.000 32
Group	H (km)	h (km)	η_0 (Pa s)	σ'_n (MPa)	n	WRSS (m^2)
Non-linear viscoelastic models						
2A	15	17	10^{21}	0.02	3	0.000 25
2B	33	107	1.2×10^{19}	0.0014	3	0.0016
Group	z (km)	η_0/w (Pa s m^{-1})	z_d	WRSS (m^2)		
Viscous afterslip models						
3	15	4×10^{15}	2.1	0.0005		
Group	z (km)	$(a-b)$	v_0 (mm yr^{-1})		σ'_{eff} (MPa km^{-1})	WRSS (m^2)
Frictional afterslip models						
4	15	0.000 36	2		20	7.3×10^{-5}
	15	0.000 72	10		20	3.4×10^{-5}
	15*	0.001*	10*		20*	0.000 59*
	15	0.000 55	20		20	4.1×10^{-5}

*Without tapered slip; see text.

stress increase, then gradually increases toward its pre-earthquake value (η_{pre}). Eq. (6) illustrates that unless the coseismic stress $\sigma_{(t,elem)}$ is of the order of σ_{pre}, the coseismic change to η_{eff} may be modest.

Mid- to lower crust (between 15 and 33 km depth) deforming with non-linear rheology is represented by the group 2A models. The group 2B models represent a non-linearly viscoelastic upper-mantle layer 33–140 km below the surface. In the results section, I discuss whether parameters required by the most successful non-linearly viscoelastic models are consistent with temperatures, stresses and rock compositions typical of continental lower crust or upper mantle.

3.3.2 *Vertical shear zones*

Shear zones extending downward from the seismogenic rupture are often idealized as creeping via stable frictional slip in the middle crust and via viscous creep at greater depths. For this project, I assume that one or the other of these processes is dominant early after an earthquake, so I model each type of after-slip separately. During each time step, horizontal shear stresses resolved on to planes tangent to the fault surface are calculated at each node, and a constitutive relationship is used to calculate the horizontal slip increment. This slip increment is added to the cumulative slip displacement for each split node and the summed slip is imposed for the following time step. In the after-slip models, all model layers are assumed to behave elastically, and after-slip may occur from the base of the coseismic rupture downward.

Velocity-dependent frictional after-slip (group 3 models) may be either stable or unstable, depending on the properties of the fault surface, temperature and other parameters. The change in friction coefficient with slip velocity is parametrized with the value $(a - b)$. If $(a - b)$ is positive, the fault zone is velocity strengthening and slip is stable. If $(a - b)$ is negative, the fault zone is velocity weakening and stick–slip behaviour occurs. Slip during each time step is calculated using the following equation (Marone *et al.*, 1991, from the equations of Dieterich (1979) or Ruina (1983)).

$$ds = dt V_0 \exp\left[\frac{d\tau}{(a-b)\sigma'_n}\right]. \quad (7)$$

V_0 is the secular slip rate, $(a - b)$ is the empirical constant relating fault friction change to change in slip velocity, σ'_n is the effective normal stress, ds is the slip per time step, τ is the time-dependent earthquake-induced shear stress resolved on to the fault surface, and dt is the time step length. This equation assumes that the steady-state value of $(a - b)$ has been attained wherever after-slip is modelled, and does not evolve with early slip. The parameter $(a - b)$ is varied, and effective normal stress σ'_n is held constant at 20 MPa km^{-1} depth. This method for modelling stable frictional after-slip is analogous to the 'hot friction' model of Linker & Rice (1997), who modelled aseismic slip following the 1989 Loma Prieta, California earthquake.

For viscous shear zone creep (group 4 models), the 'slip' (i.e. shear strain integrated across the shear zone) per time step is

$$ds = \frac{d\tau}{(\eta/w)} dt. \quad (8)$$

In eq. (8), η is viscosity, w is the horizontal width of the shear zone and the parameter η/w is varied. In crustal rocks, η should decline with increasing temperature and be only mildly sensitive to pressure, and thus should decrease with depth (z) in compositionally uniform crust. However, the rheology of the lower crust is probably controlled by feldspar rather than quartz, causing a viscosity increase in the lower crust. Also, the ratio of fault zone viscosity to that of its surroundings may decrease with depth, causing the shear zone to widen; such a widening of exhumed shear zones with depth is seen in field studies (e.g. Hanmer 1988). This widening would oppose a decrease in η/w (or $(\eta/w)_z$) with depth. Because of these uncertainties on how shear zone properties vary with depth, I focus on models in which $(\eta/w)_z$ is either uniform or decreases with depth. (Models with depth-increasing $(\eta/w)_z$ would yield after-slip concentrated just below the rupture, similar to the group 3 models.) The decrease in $(\eta/w)_z$ with depth is modelled as follows:

$$\left(\frac{\eta}{w}\right)_z = \left(\frac{\eta}{w}\right)_0 \exp\left(\frac{z-15}{z_d}\right). \quad (9)$$

In this equation, z is the depth in kilometres, z_d is a decay parameter and $(\eta/w)_0$ is the viscosity divided by the shear zone width at 15 km depth.

For both classes of vertical shear zone models, after-slip may occur wherever the fault zone was coseismically loaded by the earthquake, except in the top 15 km of the crust (where the fault was coseismically loaded beyond ends of the rupture). This last assumption is based on the fact that little or no after-slip occurred in the upper crust beyond the tips of the Izmit or Landers earthquake ruptures (e.g. Reilinger *et al.* 2002; Shen *et al.* 1994). Frictional after-slip did occur on the Izmit rupture surface itself (Hearn *et al.* 2002), but for the uniform slip case modelled here, no part of the rupture is coseismically loaded, as patches of low coseismic slip on the Izmit rupture surface were.

4 RESULTS

4.1 Models consistent with typical near-field (Station A) post-seismic displacements

4.1.1 Newtonian viscoelastic crust or mantle layers

Several viscoelastic models can approximately reproduce the Station A displacement–time curve (Fig. 5). To reproduce both the amplitude and the decay behaviour, the relaxing layer must be located at depth below the base of the earthquake rupture, and must have a low value of η. Many models from groups 1B and 1C fit the Station A displacement history to within a mean of less than 3 mm per epoch (i.e. the campaign-mode GPS 1σ error under optimal conditions). For the best group 1B and 1C models (VE-1B and VE-1C), the summed, squared residuals (SSRs) are 1.3×10^{-4} and 4.2×10^{-5} m^2, respectively, consistent with a mean misfit per 10 d epoch of 2.5 and 1 mm. (For comparison, a model with zero displacement at any time yields an SSR of 0.024 m^2, the best-fitting straight line yields an SSR of 0.0022 m^2 and curves within the shaded region in Fig. 4 yield SSRs of up to 0.012 m^2.) For each model group, sensitivity of the SSR to variations in model parameters is shown in Fig. 6.

The best group 1B model, VE-1B, requires a viscosity of 4.0×10^{16} Pa s at 25–27 km depth. One measure of characteristic stress relaxation time in models with thin viscoelastic layers is the Elsasser time (T_E), which is calculated as follows (Lehner *et al.* 1981):

$$T_E = T_M \frac{cH}{h}, \quad (10)$$

where c is $(\pi/4)^2$ and T_M (Maxwell time) is η/μ. For model VE-1B, T_E is 120 d. For the group 1C models, the best fit to the Station A displacements is obtained with a viscoelastic layer extending from 33 to 50 km depth with a viscosity of 10^{17} Pa s or $T_E \approx 35$ d. This model (VE-1C) is somewhat analogous to viscoelastic upper-mantle models proposed by Pollitz *et al.* (2001). In model VE-1C, however, the lower crust is modelled as elastic rather than as a standard linear solid, the lowest-viscosity mantle layer is much thinner, and there is no high-viscosity layer immediately below the crust.

None of the group 1A models can adequately reproduce the Station A displacement–time curve. Though the near-field post-seismic data (Fig. 3) allow a wide latitude for acceptable models, a decaying velocity with a τ_c of about 80 d and a total displacement of tens of mm after 1 yr are required. The group 1A models yield excessive

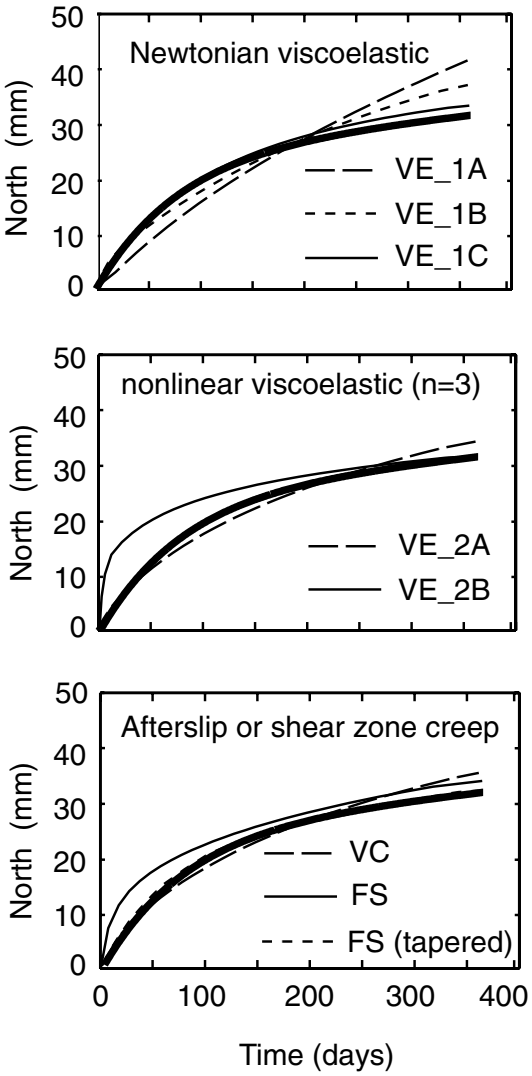

Figure 5. Modelled displacements versus time at Station A for several classes of viscoelastic relaxation and after-slip models. Top, middle and bottom figures show results from Newtonian viscoelastic, non-linear viscoelastic and after-slip models with parameters optimized to best fit the Station A displacement–time curve from Fig. 4. See the text for a description of each model.

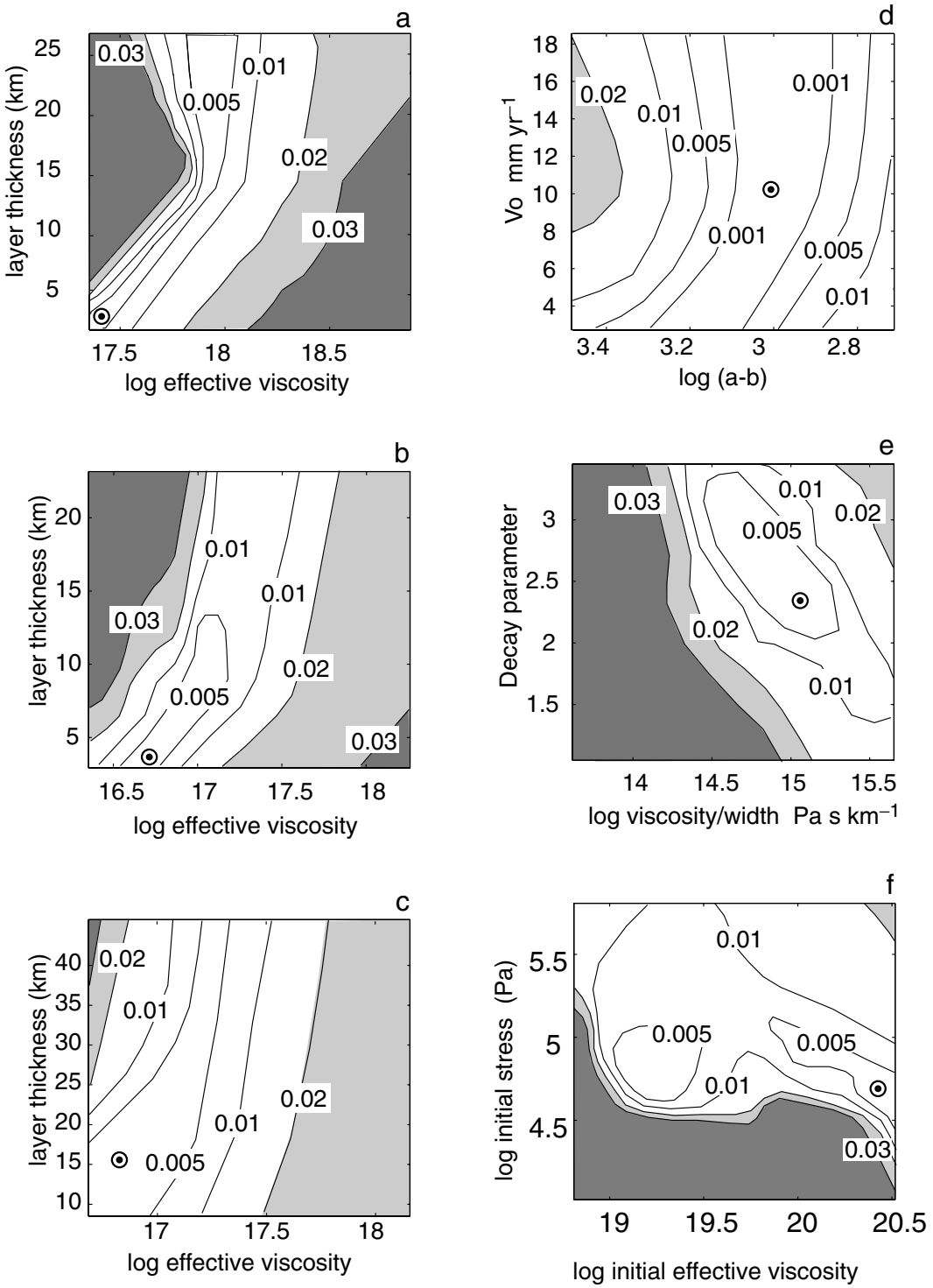

Figure 6. Sensitivity of model misfit to free parameters. Squared residuals between modelled displacements and the Station A displacement–time curve (Fig. 4) are summed over 36 10 d time intervals. (a)–(c) Group 1A, 1B and 1C linear viscoelastic models. (d) Group 3 (frictional after-slip) models, (e) group 4 (viscous shear zone creep) models, (f) group 2 (non-linear viscoelastic lower crust) models. Dots show the location in parameter space where the SSR is minimized. For comparison, a model in which Station A did not move would have an SSR of 0.024 m^2, and the best-fitting line has an SSR of 0.0022 m^2. Displacement–time curves within the shaded area in Fig. 4 have an SSR of less than 0.012 m^2.

velocities (i.e. displacements after 1 yr), if η is set low enough to yield a decaying component with $\tau_c = 80$ d. For larger values of η, the fit to the total displacement after 1 yr is improved, but the post-seismic velocities are essentially constant with time. The best group 1A model (VE-1A) fits Station A displacements only slightly better than the best-fitting line (5 mm rather than 7 mm mean misfit per epoch; the SSR is 1.0×10^{-3} m^2, compared with 2.2×10^{-3} m^2 for the best-fitting line).

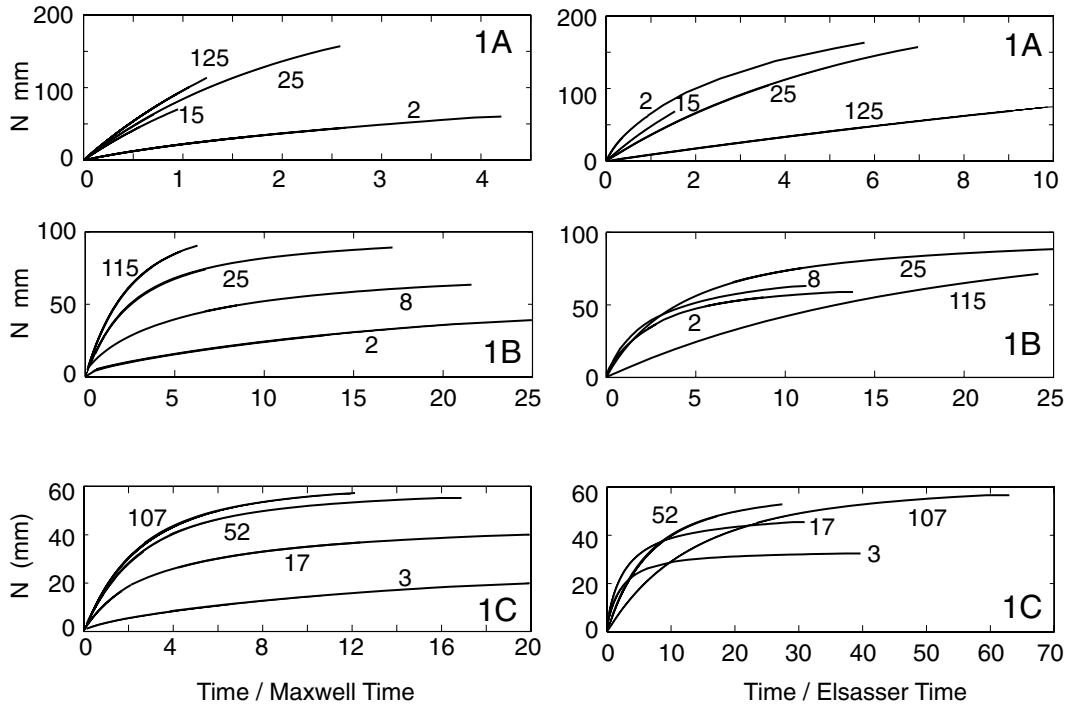

Figure 7. Station A displacements versus non-dimensionalized time for the group 1A, 1B and 1C viscoelastic models. Each curve represents a different viscoelastic layer thickness h (as labelled). If solely Maxwell time (or, for the second column, Elsasser time) governed the time dependence of near-field post-seismic deformation, only a single curve would be visible on each plot (i.e. curves for models with different values of h would be superposed).

Within model groups 1A, 1B and 1C, the evolution of surface displacements with time depends on both h and η, rather than just their ratio (which is proportional to T_E). Fig. 7 shows modelled Station A displacements plotted against non-dimensionalized time (t/T_E and t/T_M) for all of the group 1A, 1B and 1C models. If models with the same T_E yielded similar displacement histories at Station A, curves from models with different viscoelastic layer thicknesses would plot on top of each other. For models with small h, models with similar T_E yield similar (though not identical) displacements with time. For models with large h, results become increasingly similar to those predicted by layer-over-viscoelastic half-space models, for which the time dependence of deformation is characterized by T_M. For most of the models shown in Fig. 7, changes to h yield distinct displacement–time curves, regardless of how time is non-dimensionalized. This is why specific values of both h and η are specified for models VE-1B and VE-1C.

4.1.2 Non-linear crust or mantle layer

The best non-linear lower-crust model (VE-2A) with $n = 3$ fits early post-seismic displacements at Station A reasonably well: the SSR is 2.5×10^{-4}, consistent with a mean misfit per 10 d epoch of 2.5 mm. The best-fitting non-linear crust model requires σ_{pre} to be about 0.02 MPa and η_{pre} to be about 10^{21} Pa s. Although this model does not fit the Station A displacement–time curve as well as model VE-1C, models with different plate thicknesses or values of n probably could, although examining this possibility is not within the scope of this paper.

The best non-linear upper-mantle model (VE-2B) requires values of η_{pre} and σ_{pre} to be about 10^{19} Pa s and 0.001 MPa, respectively. This model yielded an SSR of 0.0016 m^2, comparable to that of the best-fitting line (0.0024 m^2), and a mean misfit per 10 d epoch of 7 mm. Thus, all of the group 2B $n = 3$ non-linear mantle models are inconsistent with the Station A post-seismic displacement history. The apparent decay time for the best-fitting model is of the order of 10–20 d and the post-seismic velocity levels off to less than 1 mm yr^{-1} within weeks of the earthquake (Fig. 5). If a higher pre-earthquake stress is modelled, the decay time for the early post-seismic deformation increases, but the amplitude becomes very small, degrading the overall fit to the Station A displacement–time curve.

4.1.3 Velocity-strengthening frictional after-slip

For $V_0 = 10$ mm yr^{-1}, the best velocity-strengthening after-slip model (FS) requires $(a - b) = 0.001$ (assuming $\sigma_n' = 20$ MPa km^{-1}). Incorporating layered elastic structure may double this estimate (e.g. Hearn *et al.* 2002) bringing it within the range of laboratory ($a - b$) estimates for creeping crustal shear zones (e.g. 0.001–0.01, Blanpied *et al.* 1995). The SSR for the best frictional after-slip model assuming $V_0 = 10$ mm yr^{-1} is 5.9×10^{-4} m^2, consistent with fitting the displacements every 10 d to within less than 3 mm. The sensitivity of the SSR to V_0 is low if $V_0 \geq 10$ mm yr^{-1} (Fig. 6).

Frictional after-slip models produce very rapid velocities immediately after an earthquake. Since even continuous GPS cannot usually capture displacements during the first hours after an earthquake (T. Herring, personal communication, 2001), the Station A displacement–time curve would not include them. Because of this, I exclude modelled displacements from the first day after the earthquake when comparing frictional after-slip model displacements to the Station A displacement history. Still, most of the misfit results from too rapid velocity decay immediately after the modelled earthquake.

The uniform-slip coseismic model yields a narrow depth interval below the dislocation with a high slip gradient and thus high shear

stress (of the order of 10 MPa). Since real earthquakes appear to have patchy slip distributions, it is uncertain whether local patches with high stress (which cause the very high initial post-seismic velocities) are present—this depends on how smooth the slip distribution is, and current seismic and geodetic slip inversion techniques do not have the resolution to answer this question. For models with a linearly tapered drop-off in slip between 10 and 15 km depth (maximum coseismic shear stress of about 2 MPa), much smaller misfits to the Station A displacement history may be obtained (3.4×10^{-5} m^2 for $V_0 = 10$ mm yr^{-1}) and the $(a - b)$ estimate is somewhat lower (3.4×10^{-5}).

4.1.4 Viscous shear zone creep

Viscous shear zone models with uniform $(\eta/w)_z$ either (1) vastly overpredict the average velocity at Station A (i.e. the displacement after 1 yr) but obtain the decay constant for the exponential term or (2) yield the correct average velocity but not the observed decay in post-seismic velocity. However, models with a step increase in $(\eta/w)_z$ at the mantle yield a better fit to the Station A displacement history. For the best viscous creep model (VC), $(\eta/w)_z$ declines from 4.0×10^{15} Pa s m^{-1} (or higher) at 15 km depth down to a minimum of 10^{12} Pa s m^{-1} at 30 km depth. Assuming the shear zone is 100 m wide at a depth of 15 km, the required shear zone effective viscosity at this depth is 4.0×10^{17} Pa s. If the shear zone width is 10 km at a depth of 30 km (e.g. Hanmer 1988), model VC requires the effective viscosity at this depth to be 10^{16} Pa s. The SSR for this model is 5.0×10^{-4} m^2, corresponding to a mean misfit of about 4 mm to the Station A displacement–time curve at each 10 d epoch. In this model, most of the early after-slip occurs at depths between 20 and 33 km.

4.2 Comparison of displacement fields

Models that can reproduce early post-seismic displacements at Station A produce distinct patterns of surface deformation elsewhere. In this section, I highlight differences in spatial and temporal patterns of surface displacements resulting from post-seismic frictional slip, viscous creep on a vertical shear zone and relaxation of viscoelastic layers.

4.2.1 Linear viscoelastic models: horizontal deformation

Fig. 8 shows total horizontal displacements after 180 d at 45 locations within $1.5L$ (i.e. 100 km) of the modelled rupture. In addition to models VE-1B and VE-1C, which on average fit displacements at Station A to within 3 mm, model VE-1A (which does not) is shown. Model VE-1A is included in Fig. 8 to illustrate how elastic layer thickness (H) influences patterns of early post-seismic deformation when near-field displacements (i.e. at Station A) are constrained to be the same. Fig. 9 shows how displacement azimuths and amplitudes vary along three transects (11′, 22′ and 33′) shown in Fig. 8.

The distance to the modelled amplitude maximum along a perpendicular transect bisecting the fault (11′; Fig. 9) appears to be approximately equal to H for most of the models, though this increases for models with thicker viscoelastic layers. For comparison, 2-D analytical solutions for an elastic plate over a viscoelastic halfspace (i.e. h and $L = \infty$) indicate that the distance to the displacement maximum within about two Maxwell times of the earthquake should be approximately $1.7H$ (Cohen 1999, Fig. 9). The difference

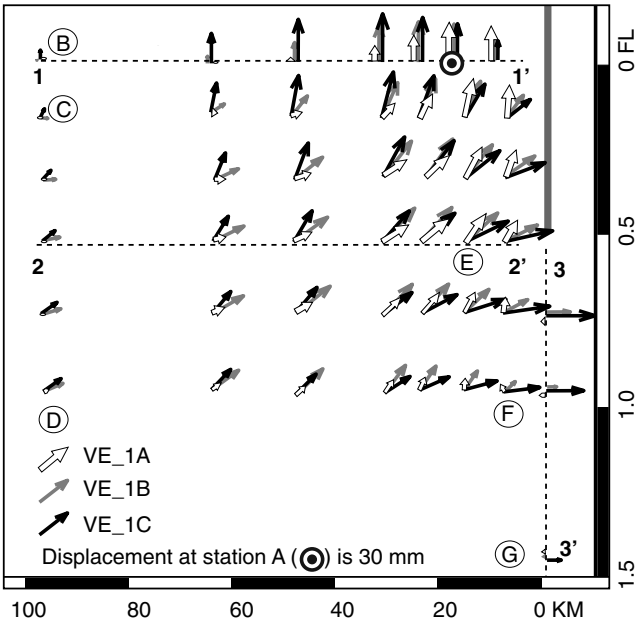

Figure 8. Horizontal displacements 80 d after the hypothetical $M_w = 7.4$ strike-slip earthquake. For this plot, group 1A, 1B and 1C model parameters are chosen to yield a displacement of 30 mm at Station A 80 d after the earthquake. Amplitudes and azimuths at other locations differ significantly for the three models.

is likely to be due to both the finite rupture length and drag on the upper crust from elastic rebound of material below the viscoelastic layer (see the discussion) in my models.

Once H is known, either from measuring the distance to the maximum fault-parallel displacement or from independent information, the maximum fault-parallel displacement along a fault-normal transect (i.e. 11′) approximately constrains T_E or T_M (for small and large h, respectively). In addition, h and η of the relaxing viscoelastic layer may estimated independently from horizontal post-seismic displacements, given either (1) precise displacement measurements along at least two transects (11′ and 33′) over a single epoch or (2) detailed, time-varying displacements at one or more judiciously chosen site locations (see below).

The first approach to estimating η and h is to compare the maximum fault-normal displacement (which occurs along strike beyond the fault tip; i.e. along a transect of 33′) to the maximum fault-parallel displacement, over a single (early post-seismic) time epoch. The maximum fault-normal displacement is much smaller than the maximum fault-parallel displacement if h is small (Fig. 10a). As h increases, the magnitudes of these displacements become more similar.

Another indicator of the η and h of the relaxing viscoelastic layer is the width of the region in which post-seismic strain is concentrated. This is defined as the distance from the rupture, along a bisecting transect, to a point where the post-seismic displacement is half of the maximum displacement along this transect. For a given H, this width ($w_{1/2}$) increases with h. Fig. 10(b) illustrates that this approach to estimating h is more diagnostic for models with large H because as H increases, the sensitivity of $w_{1/2}$ to h increases as well.

Fig. 9 shows that early post-seismic surface velocities and displacements at sites along transects of 11′ and 33′ may initially be opposite in sense to coseismic displacements if h is small. Fig. 11 shows such velocity reversals on plots of displacement versus time

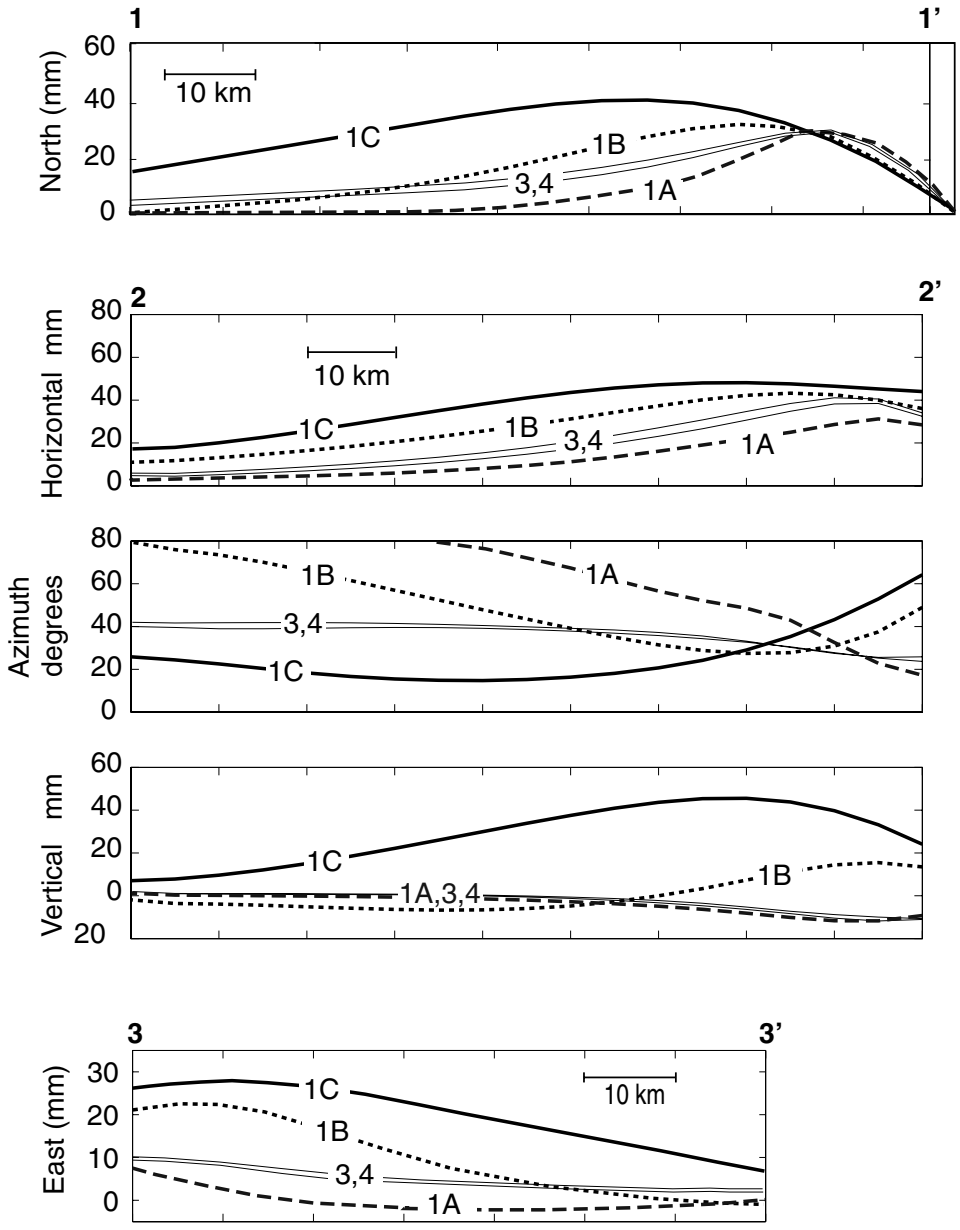

Figure 9. Modelled displacement versus distance from the rupture along transects 11′, 22′ and 33′; transect locations are shown in Fig. 8. Along transects 11′ and 33′, displacements are always fault-parallel and fault-normal, respectively, and there is no vertical motion. Along section 22′, horizontal displacement amplitude and azimuth, and vertical displacement amplitude, are shown.

(for stations B and G; locations of these and other reference locations are shown in Figs 2 and 8). In the areas surrounding transects 11′ and 33′, the fault-parallel and fault-normal components of horizontal motion, respectively, may reverse or slow during the first months after an earthquake, while the other motion component remains unaffected (e.g. Stations C and F; Appendix). This temporary effect causes some site velocity azimuths to change dramatically with time, as shown for Stations C and F on Fig. 12. Station C, which is located 100 km from the fault and just south of transect 11′ (Fig. 8), initially moves to the eastnortheast (nearly perpendicular to the rupture), but moves northerly later on. The velocity retardations or reversals are most pronounced and long lasting when H is equal to or only slightly greater than the rupture depth, and h is small.

Suppression of one horizontal motion component relative to the other may also cause displacement azimuths to vary markedly with distance from the rupture. Fig. 9 shows that along a non-bisecting transect normal to the fault (22 in Fig. 8, or any fault-normal transect between 11′ and 22′), linearly viscoelastic models can yield surface displacement azimuths that go from being essentially fault-normal far from the rupture to fault-parallel near the rupture. This is because the reversal-retardation effect is over soonest in the near field. As time progresses, variation in displacement azimuths at sites along non-rupture-bisecting transects declines. At the liquid limit for the relaxing layer, total post-seismic surface displacement patterns for models within each class (1A, 1B or 1C) are identical, depending only on rupture geometry and H. At this point, the maximum 'swing' in displacement orientations along a transect such as 22′ is $\pi/4$.

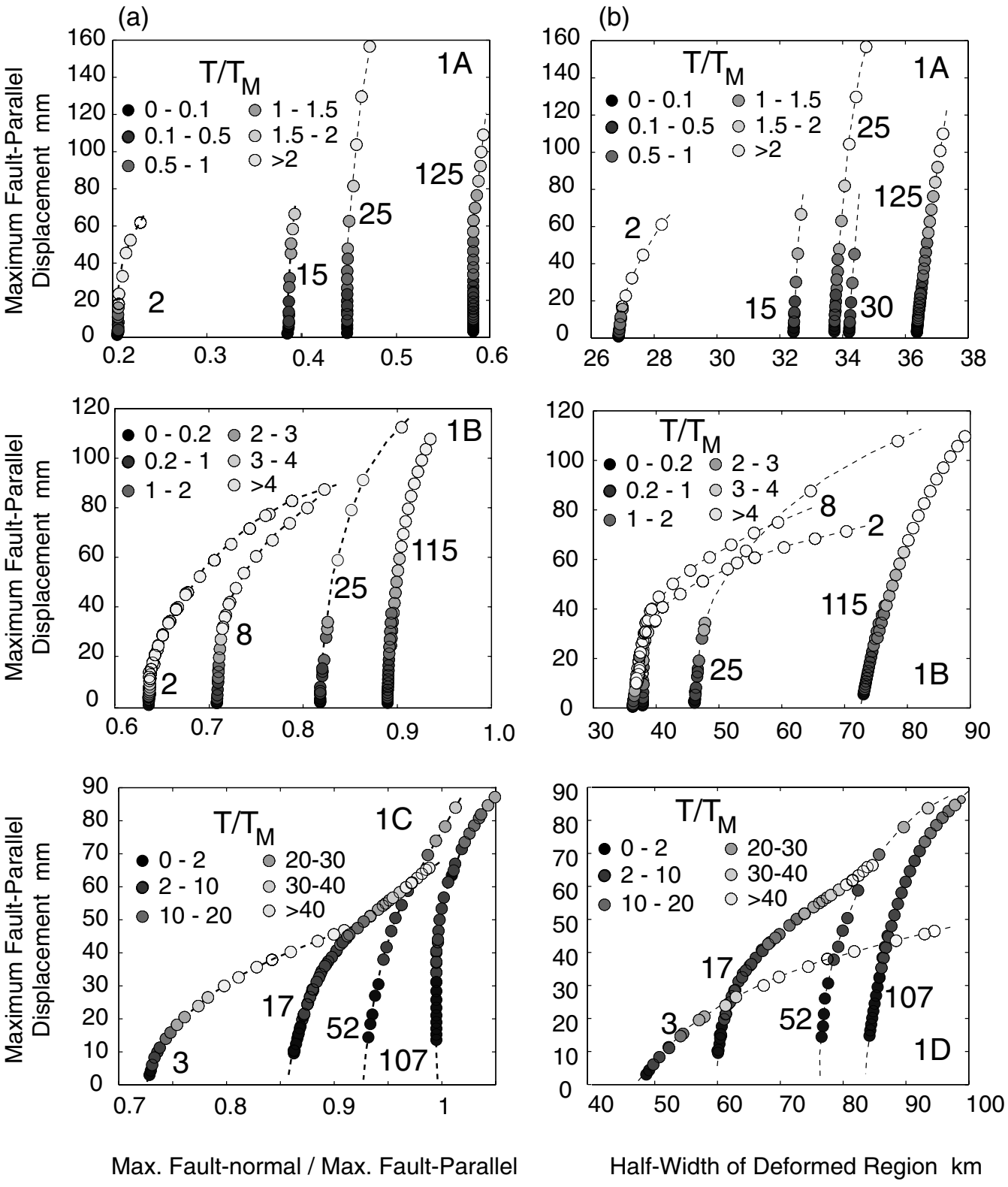

Figure 10. (a) Maximum fault-parallel displacement along 11′ plotted against the ratio of maximum fault-normal displacement (along 33′) to maximum fault-parallel displacement. Linear viscoelastic model groups 1A, 1B and 1C are shown on the top, middle and bottom plots, and each curve represents a different value of h. Shading of symbols illustrates non-dimensionalized time. Note the difference in horizontal axis scales; the group 1A models exhibit less fault-normal displacement beyond the rupture tip than group 1B and 1C models; this can also be seen in Fig. 8. (b) Maximum fault-parallel displacement along 11′ plotted against the half-width of the deforming region, ($w_{1/2}$; defined in text). For models with the smallest H (i.e. the group 1A models), early post-seismic deformation is concentrated closest to the fault; this may also be seen in Figs 8 and 9. Note that the ratio of maximum fault-normal to maximum fault-parallel displacement and $w_{1/2}$ are also sensitive to h.

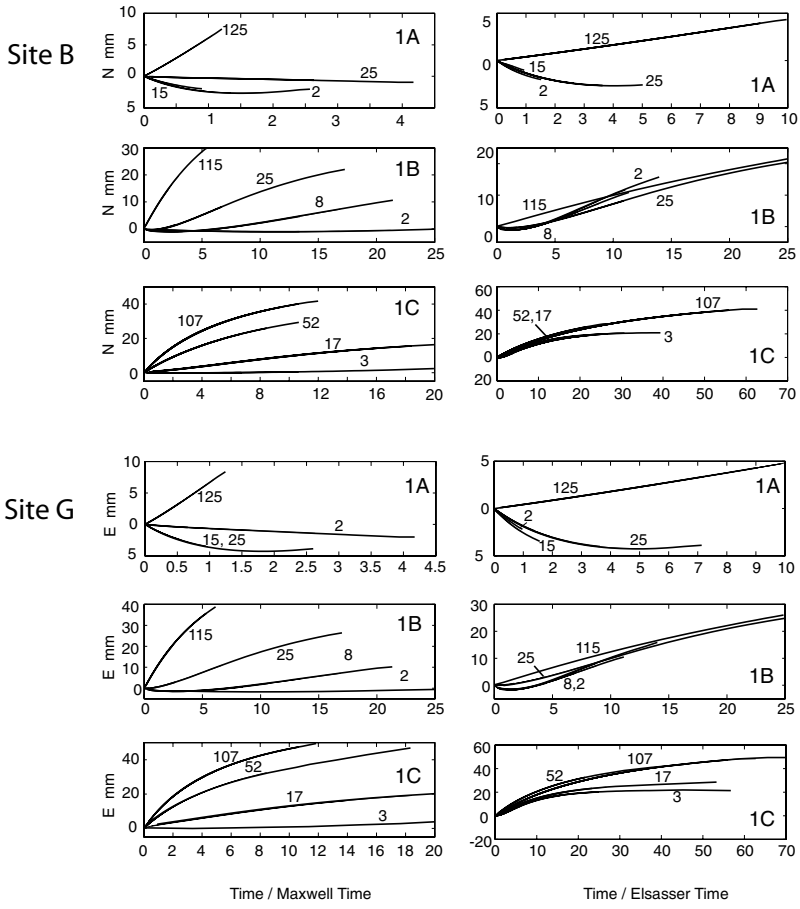

Figure 11. Displacement versus non-dimensional time (t/T_M and t/T_E) for group 1A, 1B and 1C models at hypothetical GPS sites B and G (locations shown in Figs 2 and 8). Curves represent models with different values of h. Modelled displacement–time curves for Stations C, D, E and F are included in an Appendix. Different curve lengths on these plots arise from the fact that model simulations were run for 1 yr, rather than for a set number of Elsasser or Maxwell times. (A few of the models were run for up to 7 yr.)

Detailed displacement–time data from a single site may be sufficient to estimate η and h of a relaxing viscoelastic layer, provided that h is neither very large nor very small.This is especially evident at locations such as Stations B, C, E and F (locations shown in Fig. 8), where one post-seismic velocity component is initially slowed or reversed relative to the other (Fig. 11 and the Appendix). In these locations, the displacement–time curve shape varies significantly with h over a wide range of h values, and the time dependence of velocity may be different for each horizontal component. Data from continuous GPS sites beyond a distance of about $L/2$ from the fault, and away from quadrant centres, are most likely to adequately constrain both h and η of a relaxing, linearly viscoelastic layer.

4.2.2 Linear viscoelastic models: vertical displacements

A 2-D plot of vertical displacements along transect 22′ is shown in Fig. 9 (vertical displacements along 11′ and 33′ are zero). As demonstrated by Yang & Toksöz (1981), post-seismic vertical post-seismic displacements are highly sensitive to plate thickness. As with the horizontal displacements, the distance to the maximum displacement does not change significantly with time and is a good indicator of elastic plate thickness. The polarity of this maximum displacement, however, depends on the depth of rupture penetration relative to the plate thickness (Yang & Toksöz 1981). Models VE-1B and VE-1C yield upward displacements in the near field and downward displacements in the far field, a pattern opposite to the coseismic pattern and more diffuse (analogous to Yang & Toksöz, models G1 and M1). Model VE-1A, in which the rupture completely penetrates the elastic plate, yields downward displacements throughout the quadrant, comparable to the sense of coseismic displacement in the near field (analogous to Yang & Toksöz, G2 models).

The pattern of vertical post-seismic deformation is also sensitive to viscoelastic layer thickness. Modelled displacements at Station D (see the Appendix) clearly illustrate that models with larger h produce larger upward (or smaller downward) displacements. Models with $H = 33$ km and large h produce the largest upward displacements after a given number of Maxwell times. This observation has also been made by Pollitz *et al.* (2001), who posited viscoelastic relaxation of a thick upper-mantle layer to model apparent upward post-seismic displacements in tensional quadrants following the 1992 Landers earthquake.

If vertical and horizontal displacements are both available from sites near quadrant centres, the ratio of vertical to horizontal displacement may be highly diagnostic of H and h. Modelled 3-D displacements at Station D (Appendix) show that for the group 1A models, models with large h yield small vertical displacements relative to horizontal displacements, while the opposite holds for thin layers.

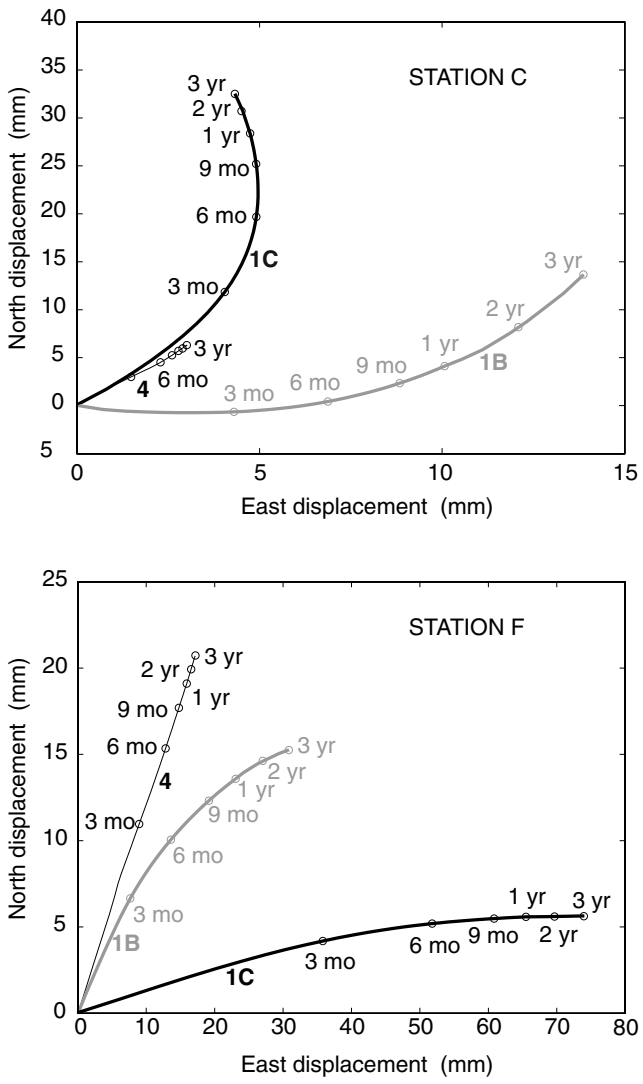

Figure 12. Motion of stations C and F over time in map view, showing rotation of velocity azimuths toward fault-parallel and fault-normal directions, respectively. Results from viscoelastic models VE-1C and VE-1B are shown. Site displacement trajectories for after-slip model VC (for which azimuth does not change significantly) are included for comparison.

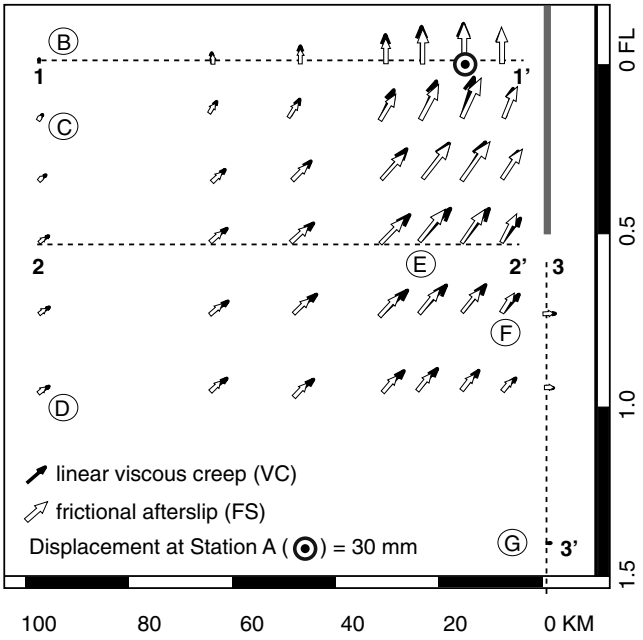

Figure 13. Modelled horizontal displacements 80 d after the hypothetical $M_w = 7.4$ strike-slip earthquake, for frictional after-slip and viscous vertical shear zone models (groups 3 and 4, respectively). Both models yield a horizontal displacement at Station A of 30 mm.

4.2.3 Non-linear viscoelastic relaxation

The best $n = 3$ non-linear lower-crust model (VE-2A) yields horizontal displacements similar to those produced by the after-slip models, with more pronounced amplitude decay away from the fault. Vertical displacements from this model are similar to those produced by model VE-1A. Distinguishing non-linear relaxation of lower crust ($n = 3$) from after-slip using GPS surface displacement data may not be straightforward, unless near-field displacement data can point to patchy after-slip on the coseismic rupture (e.g. Reilinger *et al.* 2000; Bürgmann *et al.* 2002).

4.2.4 After-slip

Fig. 13 shows modelled displacements 180 d after the earthquake for the two after-slip models, FS and VC. Horizontal azimuths and amplitudes versus distance along transect 22′, and displacements along transects 11′ and 33′, are shown in Fig. 9. These figures show that models FS and VC give similar horizontal displacements. Our modelling suggests that it is not possible to distinguish between these after-slip models based on GPS data alone. This conclusion is probably model dependent: I model uniform slip on a rectangular fault, which creates a narrow interval of high coseismic shear stress just below the rupture. For many earthquakes, however, coseismic loading is spatially patchy and can lead to after-slip on the rupture surface itself (Bürgmann *et al.* 2002; Hearn *et al.* 2002). The resulting complex patterns of near-field surface deformation could be more distinct for the two after-slip models than the results shown here.

After-slip produces post-seismic velocity azimuths that do not change as markedly with distance from the fault, or with time, as those resulting from viscoelastic relaxation. Velocities from model FS become slightly more fault-parallel with time as after-slip expands over progressively broader areas of the fault zone, but by the time this occurs, after-slip has slowed to the point where azimuth changes may be difficult to detect. Model VC yields post-seismic velocities that decay less rapidly with distance from the modelled fault than model FS, but again the differences are too small to detect with GPS (Fig. 13). Early post-seismic displacements from both the VC and FS models are more fault-parallel than the coseismic displacements. Fault-normal displacements near the end of the modelled rupture are smaller for both of the after-slip models than for the group 1B and 1C viscoelastic models, but are comparable to those produced by group 1A models with small h (Fig. 10a). This is probably due in part to after-slip or creep progressing beyond the ends of the modelled rupture, below the seismogenic zone.

Vertical displacements for the frictional after-slip and linear viscous shear zone models are shown in Fig. 9 (transect 22′). For both after-slip models, the ground surface drops in the near field (tensional quadrant), and further out, it rises slightly. In most locations, the vertical displacements are comparable to those from model

VE-1A. However, both after-slip models yield much larger downward displacements immediately adjacent to the fault (between transects 11′ and 22′ in Fig. 8) than model VE-1A.

5 DISCUSSION

5.1 Effect of *h* on stress and velocity field evolution

After-slip causes the lithosphere to move horizontally in the same direction it did during the earthquake, but viscoelastic relaxation does not. If a low-viscosity layer is present at some depth in the lithosphere, only the plate above this layer deforms post-seismically in the same sense as the earthquake. As the relaxing layer loosens its grip on the top surface of the elastic volume below it, this volume deforms in a sense opposite to coseismic as it rebounds to its pre-earthquake configuration (Fig. 14). To state this in terms of the 'jelly sandwich' lithosphere rheology model, the slice of bread below the jelly is not fixed throughout the earthquake cycle.

As the elastic volume below the viscoelastic layer deforms, it exerts drag (through the viscoelastic layer) on the upper crust, which opposes continued elastic deformation of the upper crust in the coseismic sense. This drag may cause retardation or reversal of one or both horizontal surface velocity components. Fault-parallel motion of the crust is slowed or reversed along transect 11′, and motion normal to the fault is reversed or retarded along 33′ (e.g. motion of stations B, E, F and G, Fig. 11, and Appendix). This leads to the distinct spatial and temporal character of surface deformation resulting from viscoelastic relaxation of layers with different thicknesses but identical Elsasser times. The drag may also explain why the distance to the maximum post-seismic displacement along transect 11′ is less than predicted by the analytical solution (Cohen 1999), in which an infinitely thick viscoelastic layer is assumed. Since the distinct deformation patterns for different values of *h* do not result from end effects, they will also be evident for longer ruptures. As shear stresses in the relaxing viscoelastic layer continue to decline, horizontal surface displacements approach patterns and amplitudes that depend solely on *H* and the rupture geometry.

Vertical displacements due to post-seismic viscoelastic relaxation are affected by both the elastic upper plate thickness and the thickness of the relaxing layer (e.g. Yang & Toksöz 1981; Pollitz *et al.* 2001). At a particular surface location, the vertical displacement over a post-seismic time interval is the sum of vertical strains integrated over *H*, *h* and the (essentially elastic) material below. If *h* is large, the second two terms are small. The elastic material below a thick, relaxing viscoelastic layer contributes little to the vertical displacements because it is located at a great depth and underwent little coseismic strain. Furthermore, if two models produce comparable, early post-seismic surface deformation in the near field, the model with large *h* has the lower Maxwell time and is closer to its liquid limit at any time. Thus, both volumetric strain within the relaxing layer and contributions to surface displacements from integrated vertical strain below the relaxing layer are minimized. This leaves elastic deformation of the upper plate in response to reduced shear tractions at its base as the dominant term contributing to post-seismic surface deformation. As the substrate nears its liquid limit, vertical surface displacements tend to be opposite in sense to coseismic displacements (in the near field).

On the other hand, if *h* is small (i.e. the 'jelly sandwich' crustal model), elastic deformation of material below the relaxing layer may contribute significantly to vertical displacements at the surface, particularly in the far field. Since deformation below the viscoelastic

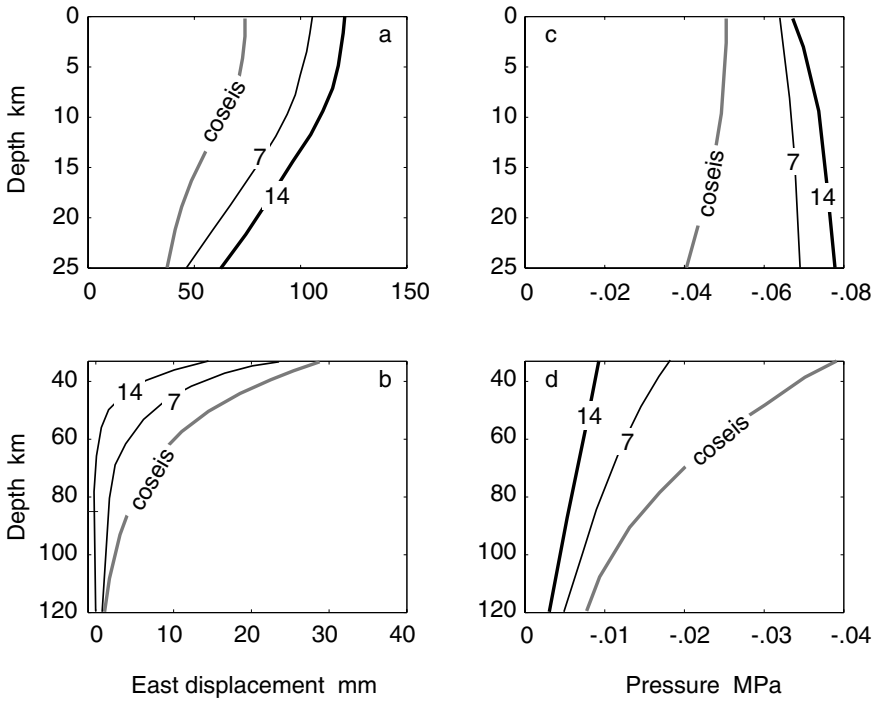

Figure 14. (a) and (b) Eastward displacement of lithosphere profiles below Station E, above and below a decoupling viscoelastic layer, for model VE-1B. Coseismic displacements, as well as displacements after 7 and 14 Maxwell times, are shown. The elastic intervals above and below the viscoelastic layer move in opposite directions as horizontal shear tractions in the decoupling layer decline over time. (c) and (d) Pressure ($(\sigma_1 + \sigma_2 + \sigma_3)/3$) as a function of depth at the same location. Coseismic deformation in tensional (pressure drops) at all depths. Post-seismically (at $t = 7\ T_M$ and $14T_M$), pressure continues to drop above the decoupling horizon, but rises in the elastic material below it. This indicates a reversed sense of deformation on either side of the relaxing layer.

layer is opposite in sense to the coseismic deformation, the sense of vertical strain at depth may be reversed relative to layer-over-viscoelastic-half-space models at the same time, and vertical displacements at the surface may also be reversed. However, since the sign of vertical strain in a volume depends on the relative magnitudes of the vertical and horizontal normal stresses, numerical calculations are required to predict vertical displacements for 'jelly sandwich' models.

Flow within the viscoelastic layer, driven by pressure gradients between compressed and dilated quadrants, could provide an alternate explanation for early post-seismic reversals in the sense of vertical motion (relative to coseismic displacements). Such flow would cause pressure changes of the same sign both above and below the relaxing layer. Examination of model VE-1B stresses shows that opposite signs of post-seismic pressure change occur above and below the relaxing layer (Fig. 14), except in the extreme near field. This shows that elastic rebound of the material below the viscoelastic layer is responsible for temporary post-seismic reversals of both vertical and horizontal surface velocity components.

5.2 How geologically reasonable are the most successful models?

In the results section, non-linear relaxation of upper mantle with $n = 3$ (group 2B models) and linear viscoelastic relaxation of the lower crust immediately below the seismogenic zone (group 1A models) were ruled out as possible causes for typical, early post-seismic deformation associated with large strike-slip earthquakes. The remaining models (viscous and frictional after-slip, viscoelastic lower crust and linearly viscous upper mantle) reproduce the Station A displacement–time curve with varying degrees of success. These models must also be judged on how consistent their required rheological parameters are with typical continental lithosphere.

5.2.1 Viscoelastic models

Model VE-1B represents linear viscoelastic relaxation of a very thin lower crustal layer or detachment, at about 25 km depth. Laboratory experiments suggest that wet quartz (Jaoul *et al.* 1984; Wang *et al.* 1994), and wet Westerly granite (Hansen & Carter 1983) could deform at the viscosity required by model VE-1B at temperatures typical for hot continental lower crust (i.e. 450–600 °C). However, free quartz is not present in typical lower crustal rocks (Rutter & Brodie 1992; Rudnick & Fountain 1995). Without free quartz (or muscovite), low viscosities could still result from shear localization, which can form thin horizons with fine grain sizes and high concentrations of volatiles, or from trapped melt along grain boundaries (Rushmer 2001). Furthermore, geophysical studies (e.g. Park *et al.* 1992; Brocher *et al.* 1994; Bokelmann & Beroza 2000) and models of topographic collapse (Kaufman & Royden 1994; Clark & Royden 2000) indicate the presence of detachments or low-viscosity crustal layers in some regions. Thus, model VE-1B could be geologically reasonable for some continental crust, particularly in regions with elevated geotherms.

Model VE-1C represents viscoelastic relaxation of either the bottom few kilometres of a thick continental crust (e.g. a model with $h = 3$ km) or a low-viscosity interval in the uppermost mantle, presumably under atypically strong crust (similar to the model of Pollitz *et al.* 2001). The relaxing material could be nearly linearly viscoelastic (e.g. a wet quartz rheology), or a non-linear material under such a large differential stress that the coseismic stress change has a negligible effect on the effective viscosity (see eq. 6) and its response to the earthquake appears to be identical to that of a linearly viscoelastic material. Assuming a wet olivine flow law (Karato & Wu 1993; Mei & Kohlstedt 2000) and high temperatures and/or differential stresses in the upper mantle, effective viscosity values required by our models (e.g. of the order of 10^{17} Pa s) can be obtained, but not under geologically tenable conditions. If the upper mantle is at 1100 °C (1400 °K), a differential stress of 100 MPa is needed to attain the required model viscosity of 10^{17} Pa s, and mantle strain rates must be of the order of 10^{-9} s^{-1}. For more typical upper-mantle temperatures, the required differential stress and strain rate are even greater. For comparison, mantle stresses have been estimated from paleopeizometric studies of xenoliths and ophiolites at 1–100 MPa, and strain rates of 10^{-12}–10^{-17} s^{-1} have been inferred from studies of olivine grain size in the upper mantle (see the summary by Carter & Tsenn 1987). The temperature and stress requirements of olivine flow laws appear to rule out mantle relaxation as a likely cause for rapid post-seismic deformation anywhere, unless a significant percentage of melt is present (e.g. Kohlstedt *et al.* 1995). It is difficult to picture why a relatively thin (17 km thick) mantle layer immediately below the crust would be significantly weaker than the surrounding lithosphere.

Model VE-1C may also represent post-seismic relaxation of quartzofeldspathic lower crust in areas with high crustal thickness. The effective viscosity required by model VE-1C (10^{17} Pa s) is consistent with a quartz-controlled (linear) rheology in hot lower crust (i.e. 500–600 °C), and may be geologically reasonable in some regions. However, non-linear flow laws for more typical lower crustal rocks (in which feldspar is the rate-controlling component) do not yield the required effective viscosity at stresses of less than about 100 MPa (e.g. Shelton & Tullis 1981; Caristan 1982). For such a low-viscosity material to maintain differential stresses of 100 MPa, the strain rate would have to be unreasonably high for the lower crust (10^{-9} s^{-1}).

Non-linear lower-crust model VE-2A reproduces the reference displacements at Station A reasonably well, given $\eta_{\rm pre}$ of the order of 10^{21} Pa s and $\sigma_{\rm pre}$ of the order of 2 to 5 $\times$ 10^4 Pa (implying a very low strain rate in the lower crust). As Fig. 6 illustrates, these parameters must be finely tuned. Immediately after the earthquake, when the differential stress increases by a few MPa in the near field, the effective viscosity of the lower crust in that area must decline to 10^{17} Pa s. Non-linear flow laws for feldspathic rocks suggest that at 500–600 °C, differential stresses of the order of 100 MPa are required to obtain $\eta_{\rm eff} \approx 10^{17}$ Pa s. This vastly exceeds the maximum coseismic stress change in the lower crust, so coseismic weakening of non-linearly viscoelastic lower crust (with $n \approx 3$) is probably not responsible for rapidly decaying, early post-seismic deformation. However, a suite of non-linear models with n between 1 and 3 and H between 15 and 25 km could be devised to reproduce early post-seismic displacements at Station A. Values of $\eta_{\rm pre}$ and $\sigma_{\rm pre}$ for some of these models could be compatible with known flow laws for crustal rocks.

5.2.2 After-slip models

The frictional after-slip model FS requires a value of velocity-strengthening parameter $(a - b)$ that is at the bottom of the range for velocity-strengthening crust below the seismogenic zone. Low $(a - b)$ values have been estimated from an analysis of post-seismic data from both the Loma Prieta, California and Izmit, Turkey earthquakes (e.g. Linker & Rice 1997; Hearn *et al.* 2002). One interpretation is that the product $(a - b)\sigma_n'$ is low because σ_n' is small. This could happen if pore pressures in the fault zone were high enough to

significantly reduce the effective normal stress. Another possibility is that a two-state variable evolution of the friction parameter may keep $(a - b)$ small and positive, particularly where temperatures are 350–500 °C (e.g. Blanpied *et al.* 1995). There is not much constraint on acceptable $(a - b)$ values in shear zones (particularly at depth) because of scarce and somewhat scattered experimental estimates, and because $(a - b)$ is highly sensitive to temperature and other parameters. This means that the 'geologically reasonable' standard is (currently) met for continental crust in nearly any part of the world.

Most estimates of the velocity-strengthening parameter $(a - b)$ at mid-crustal conditions (e.g. Blanpied *et al.* 1995) are too high to permit enough after-slip to cause rapid post-seismic deformation. If these estimates are accurate, rapidly decaying post-seismic deformation could still result from viscous creep on a vertical shear zone extending deep into the crust. Assuming a 10 km wide shear zone in the mid to lower crust (consistent with field observations of exhumed shear zones, e.g. Hanmer 1988), the required viscosity for our best VC model is about 10^{17} Pa s. If the rate of creep in the shear zone is controlled by quartz, and if sufficient volatiles are present, this viscosity could be achieved at temperatures of 450–600 °C (Wang *et al.* 1994). These temperatures are not unreasonable for the lower continental crust in areas of moderate to high heat flow (e.g. Lachenbruck & Sass 1977), but free quartz is uncommon in typical lower crustal rocks (e.g. Rudnick & Fountain 1995). However, fluid-assisted mechanisms such as grain boundary diffusion or sliding are common aseismic deformation process in crustal shear zones (Kirby 1983; Carter & Tsenn 1987), and might be at least partly responsible for rapid post-seismic deformation. Since these viscous processes permit thrust faults and normal faults to merge into near-horizontal detachment surfaces in the middle crust (i.e. in varied tectonic settings), they could also control the rheology of strike-slip faults at mid-crustal depths.

Since strikingly similar episodes of rapid post-seismic deformation have been observed in many parts of the world, a single explanation for this deformation has to hold for a wide range of geological settings. Models incorporating frictional after-slip and viscous creep along shear zones do not require fine tuning with respect to input parameters to produce early near-field post-seismic deformation typical of large strike-slip earthquakes. Frictional slip and fluid-assisted viscous creep are also known to occur in a wide variety of geological settings. On the other hand, input parameters for successful viscoelastic models (such as VE-1B and VE-1C) require η_{eff} values that are reasonable only for hot crust containing abundant quartz and volatiles. Thus, models FS and VC appear to provide the most geologically reasonable explanation of early post-seismic deformation following large earthquakes. (This conclusion does not rule out models of processes or rheologies not dealt with here, such as biviscous rheology (Ivins 1996) or transient elasticity evolution (e.g. O'Connell & Budiansky 1974).) Analysis and interpretation of detailed GPS data from future large earthquakes will resolve the question of whether low-viscosity layers in the crust or mantle contribute significantly to early post-seismic deformation. The next section suggests how to monitor such deformation, principally to distinguish between after-slip and linear viscoelastic relaxation of crust or mantle layers.

5.3 Optimal monitoring of post-seismic deformation transients

To distinguish between after-slip and relaxation of viscoelastic layers (with various values of H and h), either spatially detailed 'snapshots' of early post-seismic displacements at many sites, or precise measurements of evolving post-seismic displacements at fewer sites, may be sufficient.

5.3.1 Many sites, few time intervals

To distinguish between the processes I have examined here using spatially dense data, horizontal displacements from at least two transects should be available. One should be a fault-normal transect crossing the rupture and the other, a fault-parallel transect extending along strike along and beyond the end of the rupture (Fig. 15). Both must be long enough to define the width of the region with observable post-seismic displacements (to a distance of $2L$ from the rupture). Since the ratio of maximum fault-normal to maximum fault-parallel displacement is important for identifying h and η for a relaxing layer (Fig. 10a), high-precision measurements are required (because to calculate the error associated with this ratio, the relative measurement errors of the numerator and the denominator are summed). Displacements from sites closest to the fault along 11′ are most useful for identifying the distance from the fault to the post-seismic displacement maximum, which can be used to estimate H.

If a fault-normal transect does not exactly bisect the earthquake rupture but is close to one end, the ratio of maximum fault-parallel displacement along this transect to the maximum fault-normal displacement along 33′ may still be used to good effect. Fig. 9 shows that the differences in maximum amplitudes along transects 11′ and 22′ are not great. The least useful locations for horizontal displacement measurements are in the centres of the P and T quadrants, where both after-slip and viscoelastic relaxation models yield similar displacement azimuths that do not vary much with time. Differences between surface displacement patterns predicted by the linear viscoelastic relaxation models are at a maximum within a few Maxwell times of the earthquake, so early deployment is essential to characterize an unusually low-viscosity layer. The same is

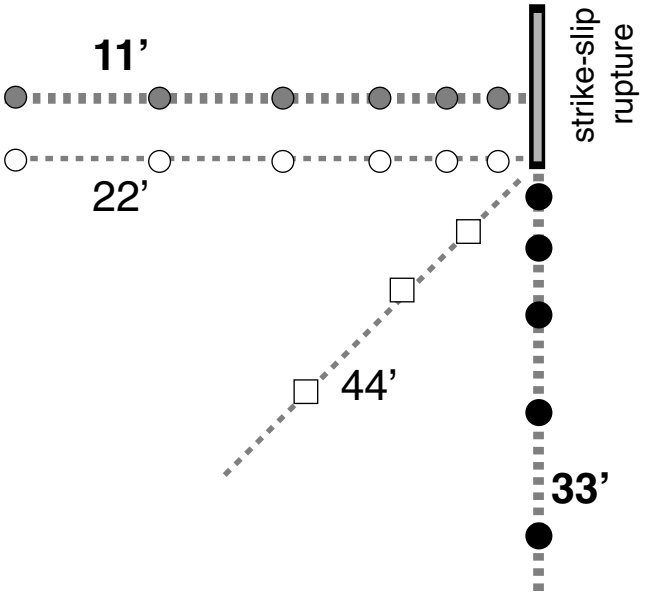

Figure 15. Ideal GPS site locations for monitoring post-seismic deformation, with the goal of distinguishing after-slip from relaxation of linearly viscoelastic layers, or identifying h and η of a relaxing viscoelastic layer. Transects 11′ (or 22′) and 33′ are the most important for providing diagnostic, horizontal displacement data. Vertical displacements are at a maximum along transect 44″, but horizontal displacement azimuths along this transect are similar for after-slip and viscoelastic relaxation models (i.e. not diagnostic).

true for characterizing after-slip, which may decay rapidly after an earthquake (e.g. Tse & Rice 1986; Marone *et al.* 1991; Bürgmann *et al.* 2002; Hearn *et al.* 2002). In general, measurement precision is important, so GPS sites where pre-earthquake velocities are well quantified (and hence where errors to corrections for secular deformation are small) should be monitored frequently, even if their locations are not ideal.

In contrast to horizontal displacements, the maximum differences between modelled vertical displacements occur at the centres of *P* and *T* quadrants. A transect of continuous GPS stations extending diagonally outward from the rupture tip could define vertical displacement as a function of distance to the fault. (InSAR interferograms, on the other hand, are a poor proxy for a map of vertical displacements because for strike-slip earthquakes, range changes reflect mostly horizontal motion.) The interpretation of vertical displacements is complicated by the fact that the sign of these displacements (up or down) changes with time at different rates in most areas (except the near field, where poroelastic deformation and irregularities in slip distribution may make interpretation challenging anyway). Shallow viscoelastic relaxation and after-slip also yield similar vertical displacements (Fig. 9). Given typical measurement errors for vertical displacements, it is unlikely that one of the aseismic deformation scenarios presented here could be distinguished from the others based solely on vertical displacements, except for linear relaxation of the mantle (see Fig. 9, transect 22′). Vertical and horizontal displacements together may be diagnostic, particularly for identifying viscoelastic relaxation of lower crust or upper-mantle layers, but interpretation of such data requires detailed numerical modelling because of the extreme sensitivity of vertical displacements to small changes in h, H, rupture depth and location.

5.3.2 Temporally detailed data from a few GPS sites

Detailed measurements of time-varying velocities at a few GPS sites may provide enough information to at least rule out several candidate models. Data from sites in the intermediate to far field along transects 33′ and 11′ (or 22′) are the most useful for discerning between viscoelastic relaxation models. The principal rule is, avoid the centres of *P* and *T* quadrants.

Time-dependent displacement data from GPS sites at *P*–*T* quadrant centres or adjacent to the fault may provide only limited constraints for viscoelastic models because several non-unique combinations of h and η may adequately explain displacement–time curves at those locations. At most sites along transect 22′, and in other areas not close to quadrant centres, one of the horizontal components (fault-parallel or fault-normal) is initially slowed or reversed. This leads to velocity azimuth rotation with time (Fig. 12), which may be modelled to estimate both h and η. In general, velocity azimuths at sites along strike (or in that vicinity, e.g. Stations E and F) become increasingly fault-normal with time if viscoelastic layer relaxation is occurring, and velocities of sites just off the bisecting transect (e.g. Station C) gradually become more fault parallel. Since after-slip yields fault-parallel and fault-normal velocity components with a similar time dependence, decaying post-seismic velocities with unchanging azimuths at sites positioned like Stations C, E and F indicate after-slip. If continuous GPS data are available from sites at different distances from the rupture, comparing apparent τ_c is instructive: increases to tau_c with distance from the rupture signal viscoelastic relaxation rather than after-slip. Also, if spatially detailed displacement data show strain concentrated around the rupture and appear consistent with either after-slip or viscoelastic relaxation with $H \approx 15$ km, continuous GPS data may prove decisive. In this case, rapidly decaying surface velocities ($\tau_c \approx 80$ d) would indicate after-slip and near-constant velocities would indicate viscoelastic relaxation.

5.3.3 Real earthquakes

Each earthquake presents its own set of logistical challenges for GPS monitoring, and measuring time-dependent post-seismic displacements in the areas shown in Fig. 15 (and near pre-existing GPS sites where secular velocity corrections can be made) may be impossible. In addition, ideal monitoring strategies depend on which phenomenon is to be characterized (which is unknown beforehand). Characterizing relaxing viscoelastic relaxation lower crust or mantle layers, or telling after-slip from viscoelastic relaxation, has been the focus of the previous section, and recommendations for monitoring post-seismic deformation with this in mind were given above. However, if the focus is on the dynamics of after-slip (e.g. Hearn *et al.* 2002) then GPS sites are close to the rupture, where they may not provide much useful information on anything else.

To some extent, the questions that can be adequately answered from modelling post-seismic deformation may be serendipitous, depending on where GPS displacement measurements can be made after a particular earthquake. However, since one contentious question among earthquake scientists is whether or not significant relaxation of the upper mantle is redistributing stresses over large areas during the years following large earthquakes, efforts should be made to design post-seismic GPS networks to answer this question. To do so, the network must include several sites along strike beyond the rupture tip (not just along transects crossing the rupture), and frequent (or continuous) monitoring of distant sites is as important as (or more important than) frequent monitoring of sites near the rupture.

6 CONCLUSIONS

Several after-slip and viscoelastic relaxation models adequately reproduce early, near-field post-seismic displacements typical of large strike-slip earthquakes, including their time dependence (i.e. velocity decay). However, modelled displacements away from the reference point are distinct and may evolve with time, particularly for models incorporating relaxation of linearly viscoelastic layers. GPS data from either continuous or frequently monitored campaign-mode sites in well-chosen locations may be sufficient to resolve the cause of post-seismic deformation (i.e. after-slip versus relaxation of linearly viscoelastic layers), and, for a relaxing Newtonian layer, to resolve both its viscosity and its thickness.

GPS sites should not be concentrated adjacent to the rupture if the object of monitoring is to identify possible relaxation of linearly viscoelastic mantle or lower crust. In this case, the best locations for GPS sites are along fault-parallel transects extending at least one fault length beyond the ends of the rupture (transect 33′ in Fig. 15), and along another transect crossing the rupture (transects 11′ and 22′ in Fig. 15).

The ‘smoking gun’ for relaxation of linearly viscoelastic layers at depth (i.e. $H = 25+$ km) is a large component of fault-normal motion at sites beyond the rupture tip. (A broad region of high strain ($w_{1/2}$) and uplift of extensional quadrants in the near field are also diagnostic.) Post-seismic velocity azimuths that change dramatically over time (due to differences in time dependence of the fault-normal and fault-parallel velocity components) indicate relaxation of a thin, linearly viscoelastic layer or horizontal shear zone. If GPS site velocity azimuths do not change with time, and if horizontal velocities decay at a comparable rate at all distances from the rupture, then

of the processes modelled here, after-slip (or perhaps relaxation of non-linear material in the mid to lower crust) is most likely. Small fault-normal displacements near and beyond the fault tip also suggest that relaxation of linearly viscoelastic layers at depth below the rupture is not occurring.

Two classes of models I developed for this study could not produce time-dependent near-field displacements typical of large strike-slip earthquakes: linearly viscoelastic models with $H = 15$ km (group 1A) and non-linearly viscoelastic models with $n = 3$ and $H = 33$ km (group 2B). Though the target displacement–time curve is not too well constrained (Fig. 4), data from the three earthquakes still require a decaying transient with a characteristic time of the order of 80 d, and a total displacement after 1 yr of the order of tens of millimetres. Models from groups 1A and 2B cannot meet both requirements. Furthermore, the η_{eff} value required by model VE-1C requires a geologically unreasonable strain rate of the order of 10^{-9} s^{-1} in the upper mantle (assuming a hot upper mantle and a wet peridotite flow law). This suggests that rapid viscoelastic relaxation is more likely to occur in the lower crust rather than in the upper mantle.

ACKNOWLEDGMENTS

This research was supported by the Southern California Earthquake Center. SCEC is funded by NSF Cooperative Agreement EAR-0106924 and USGS Cooperative Agreement 02HQAG0008. The SCEC contribution number for this paper is 716. I would like to thank Fred Pollitz and Shoichi Yoshioka for their comments on the manuscript. I would also like to thank Brad Hager and Roland Bürgmann for their suggestions on earlier drafts of this paper.

REFERENCES

Blanpied, M.L., Lockner, D.A. & Byerlee, J.D., 1995. Frictional slip of granite at hydrothermal conditions, *J. geophys. Res.,* **100,** 13 045–13 064.

Bock, Y. *et al.*, 1997. Southern California Permanent GPS Array: continuous measurements of regional crustal deformation between the 1992 Landers and 1994 Northridge Earthquakes, *J. geophys. Res.,* **102,** 18 013–18 033.

Bokelmann, G. & Beroza, G., 2000. Depth-dependent earthquake focal mechanism orientations: evidence for a weak zone in the lower crust, *J. geophys. Res.,* **105,** 21 683–21 695.

Brocher, T.M., McCarthy, J., Hart, P.E., Holbrook, W.S. & Furlong, K.P., 1994. Seismic evidence for a lower crustal detachment beneath San Francisco Bay, California, Science, **265,** 1436–1439.

Bürgmann, R., Ergintav, S., Segall, P., Hearn, E.H., McClusky, S., Reilinger, R.E., Woith, H. & Zschau, J., 2002. Time–space variable afterslip on and deep below the Izmit earthquake rupture, *Bull. seism. Soc. Am.,* **92,** 126–137.

Caristan, Y., 1982. The transition from high-temperature creep to fracture in Maryland Diabase, *J. geophys. Res.,* **87,** 6781–6790.

Carter, N.L. & Tsenn, M.C., 1987. Flow properties of continental lithosphere, *Tectonophysics,* **136,** 27–63.

Clark, M.K. & Royden, L.H., 2000. Topographic ooze: building the eastern margin of Tibet by lower crustal flow, *Geology,* **28,** 703–706.

Cohen, S.C., 1999. Numerical models of crustal deformation in seismic zones, *Adv. Geophys.,* **41,** 133–231.

Deng, J., Gurnis, M., Kanamori, H. & Hauksson, E., 1998. Viscoelastic flow in the lower crust after the 1992 Landers, California earthquake, *Science,* **282,** 1689–1692.

Dieterich, J.H., 1979. Modeling of rock friction 1. Experimental results and constitutive equations, *J. geophys. Res.,* **84,** 2161–2168.

Ergintav, S., Bürgmann, R., McClusky, S., Cakmak, R., Reilinger, R.E., Lenk, O., Barka, A. & Gurkan, O., 2002. Postseismic deformation near the Izmit earthquake 17 August, 1999, *Bull. seism. Soc. Am.,* **92,** 194–207.

Freed, A.M. & Lin, J., 2001. Delayed triggering of the 1999 Hector Mine earthquake by viscoelastic stress transfer, *Nature,* **411,** 180–183.

Gomberg, J. & Ellis, M., 1994. Topography and tectonics of the central New Madrid seismic zone: results of numerical experiments using a three-dimensional boundary-element program, *J. geophys. Res.,* **99,** 20 299–20 310.

Hanmer, S., 1988. Great Slave Lake shear zone, Canadian Shield: reconstructed vertical profile of a crustal scale fault zone, *Tectonophysics,* **149,** 245–264.

Hansen, F.D. & Carter, N.L., 1983. Semibrittle creep of dry and wet Westerly Granite at 1000 MPa, *24th US Symp. on Rock Mechanics,* Texas A&M University, College Station, TX.

Hearn, E.H., Bürgmann, R. & Reilinger, R., 2002. Dynamics of Izmit earthquake postseismic deformation and loading of the Düzce earthquake hypocenter, *Bull. seism. Soc. Am.,* **92,** 172–193.

Heki, K.S., Miyazaki, S. & Tsuji, H., 1997. Silent slip following an interplate thrust earthquake at the Japan Trench, *Nature,* **386,** 595–598.

Hsu, Y.-J., Bechor, N., Segall, P., Yu, S.-B. & Ma, K.-F., 2002. Rapid afterslip following the 1999 Chi-Chi, Taiwan earthquake, *Geophys. Res. Lett.,* **29,** 10.1029/2002GL014967.

Ivins, E.R., 1996. Transient creep of a composite lower crust, 2. A polymineralic basis for rapidly evolving postseismic deformation modes, *J. geophys. Res.,* **101,** 28 005–28 028.

Jaoul, O., Tullis, T. & Kronenburg, A., 1984. The effect of varying water contents on the creep behaviour of Heavitree quartzite, *J. geophys. Res.,* **89,** 4298–4312.

Karato, S.-I. & Wu, P., 1993. Rheology of the upper mantle: a synthesis, *Science,* **260,** 771–778.

Kaufman, P.S. & Royden, L.H., 1994. Lower crustal flow in an extensional setting: constraints from the Halloran Hills region, eastern Mojave Desert, *J. geophys. Res.,* **99,** 15 723–15 739.

Kenner, S.J. & Segall, P., 2000. Postseismic deformation following the 1906 San Francisco earthquake, *J. geophys. Res.,* **105,** 13 195–13 209.

Kirby, S.H., 1983. Rheology of the lithosphere, *Rev. Geophys. Space Phys.,* **21,** 1458–1487.

Kohlstedt, D.L., Evans, B. & Mackwell, S.J., 1995. Strength of the lithosphere: constraints imposed by laboratory experiments, *J. geophys. Res.,* **100,** 17 587–17 602.

Lachenbruck, A.H. & Sass, J.H., 1977. Heat flow in the United States and the thermal regime of the crust, *Geophys. Monograph,* **20,** 626–675.

Lehner, F.K., Li, V.C. & Rice, J.R., 1981. Stress diffusion along plate boundaries, *J. geophys. Res.,* **86,** 6155–6169.

Linker, M.F. & Rice, J.R., 1997. Models of postseismic deformation and stress transfer associated with the Loma Prieta earthquake, in US Geological Survey Professional Paper 1550-D: the Loma Prieta Earthquake of October 17, 1989; aftershocks and postseismic effects, pp. D253–D275.

McClusky, S. *et al.*, 2000. Global Positioning System constraints on plate kinematics and dynamics in the Eastern Mediterranean and Caucasus, *J. geophys. Res.,* **105,** 5695–5719.

McClusky, S.C., Bjornstad, S.C., Hager, B.H., King, R.W., Meade, B.J., Miller, M.M., Monastero, F.C. & Souter, B.J., 2001. Present day kinematics of the Eastern California Shear Zone from a geodetically constrained block model, *Geophys. Res. Lett.,* **28,** 3369–3372.

Marone, C.J., Scholz, C.H. & Bilham, R., 1991. On the mechanics of earthquake afterslip, *J. geophys. Res.,* **96,** 8441–8452.

Meade, B., Hager, B., McClusky, S., Reilinger, R.E., Ergintav, S., Lenk, O., Barka, A. & Ozener, H., 2002. Estimates of seismic potential in the Marmara Sea region from block models of secular deformation constrained by GPS measurements, *Bull. seism. Soc. Am.,* **92,** 208–215.

Mei, S. & Kohlstedt, D.L., 2000. Influence of water on plastic deformation of olivine aggregates 2. Dislocation creep regime, *J. geophys. Res.,* **105,** 21 471–21 481.

Melosh, H.J. & Raefsky, A., 1981. A simple and efficient method for introducing faults into finite element computations, *Bull. seism. Soc. Am.,* **71,** 1391–1400.

Nur, A. & Mavko, G., 1974. Postseismic viscoelastic rebound, *Science,* **183,** 204–206.

O'Connell, R.J. & Budiansky, B., 1974. Seismic velocities in dry and saturated cracked solids, *J. geophys. Res.,* **79,** 5412–5426.

Owen, S. *et al.*, 2002. Early postseismic deformation from the $M_w = 7.1$ Hector Mine, California, earthquake as measured by survey mode GPS, *Bull. seism. Soc. Am.,* **92,** 1423–1432.

Park, S.K., Kinn, C.L. & Jiracek, G.R., 1992. Magnetotelluric evidence for the brittle–ductile transition beneath the Peninsular Ranges Batholith, Southern California, *EOS, Trans. Am. geophys. Un. Fall Meeting Abs.,* **73** (43 suppl.), 313.

Pollitz, F.F., 1997. Gravitational viscoelastic postseismic relaxation on a layered spherical earth, *J. geophys. Res.,* **102,** 17 921–17 941.

Pollitz, F.F., Peltzer, G. & Bürgmann, R., 2001. Mobility of continental mantle: evidence from postseismic geodetic observations following the 1992 Landers earthquake, *J. geophys. Res.,* **105,** 8035–8054.

Reilinger, R.E. *et al.*, 2002. Coseismic and postseismic fault slip for the 17 August 1999, $M = 7.5$, Izmit, Turkey earthquake, *Science,* **289,** 1519–1524.

Rice, J.R., 1980. The mechanics of earthquake rupture, in *Physics of the Earth's Interior, Proc. Int. School of Physics 'Enrico Fermi', Course LXXVIII,* **78,** 555–649.

Rudnick, R.L. & Fountain, D.M., 1995. Nature and composition of the continental lower crust: a lower crustal perspective, *Rev. Geophys.,* **33,** 267–309.

Rushmer, T., 2001. Volume change during partial melting reactions: implications for melt extraction, melt geochemistry, and crustal rheology, *Tectonophysics,* **342,** 389–405.

Ruina, A., 1983. Slip instability and state variable friction laws, *J. geophys. Res.,* **88,** 10 359–10 370.

Rutter, E.H. & Brodie, K.H., 1992. Rheology of the lower crust, in *Continental Lower Crust,* pp. 201–267, eds Fountain, D.M., Arculus, R.& Kay, R.W., Elsevier, Amsterdam.

Saucier, F. & Humphreys, E.D., 1993. Horizontal crustal deformation in Southern California from joint models of geologic and very long baseline interferometry measurements, in *Contributions of Space Geodesy to Geodynamics,* Vol. 23, pp. 139–176, eds Smith, D.E. & Turcotte, D.L., AGU Geodyn. Ser., Washington, DC.

Saucier, F., Humphreys, E.D. & Weldon, R.J., 1992. Stress near geometrically complex strike-slip faults: application to the San Andreas Fault at Cajon Pass, southern California, *J. geophys. Res.,* **97,** 5081–5094.

Savage, J.C. & Svarc, J.L., 1997. Postseismic deformation associated with the 1992 $M_w = 7.3$ Landers earthquake, southern California, *J. geophys. Res.,* **102,** 7565–7577.

Shelton, G. & Tullis, J., 1981. Experimental flow laws for crustal rocks, *EOS, Trans. Am. geophys. Un.,* **62,** 396.

Shen, Z.-K., Jackson, D.D., Feng, Y., Cline, M., Kim, M., Fang, P. & Bock, Y., 1994. Postseismic deformation following the Landers earthquake, California, 28 June 1992, *Bull. seism. Soc. Am.,* **84,** 780–791.

Souter, B.J., 1998. Comparisons of geological models to GPS observations in Southern California, MIT, *PhD thesis*.

Thatcher, W., 1983. Nonlinear strain buildup and the earthquake cycle on the San Andreas Fault, *J. geophys. Res.,* **88,** 5893–5902.

Tse, S.T. & Rice, J.R., 1986. Crustal earthquake instability in relation to the depth variation of frictional slip properties, *J. geophys. Res.,* **91,** 9452–9472.

Wang, J.N., Hobbs, B.E., Ord, A., Shimamoto, T. & Torumi, M., 1994. Newtonian dislocation creep in quartzites: implications for rheology of the lower crust, *Science,* **265,** 1204–1205.

Webb, F. & Melbourne, T., 1996. GPS observations of rapid postseismic deformation in subduction zones *EOS, Trans. Am. geophys. Un.,* **77,** 518.

Yang, M. & Toksöz, M.N., 1981. Time-dependent deformation and stress relaxation after strike-slip earthquakes, *J. geophys. Res.,* **86,** 2889–2901.

Yu, T.-T., Rundle, J.B. & Fernandez, J., 1996. Surface deformation due to a strike-slip fault in an elastic gravitational layer overlying a viscoelastic gravitational half-space, *J. geophys. Res.,* **101,** 3199–3214.

APPENDIX: MODELLED SITE DISPLACEMENTS VERSUS NON-DIMENSIONALIZED TIME

This appendix contains plots of modelled post-seismic displacements versus non-dimensionalized time for site D, E and F. They are essentially a continuation of Figure 11, at sites where non-zero post seismic displacements were predicted for all three motion components (E, N and U).

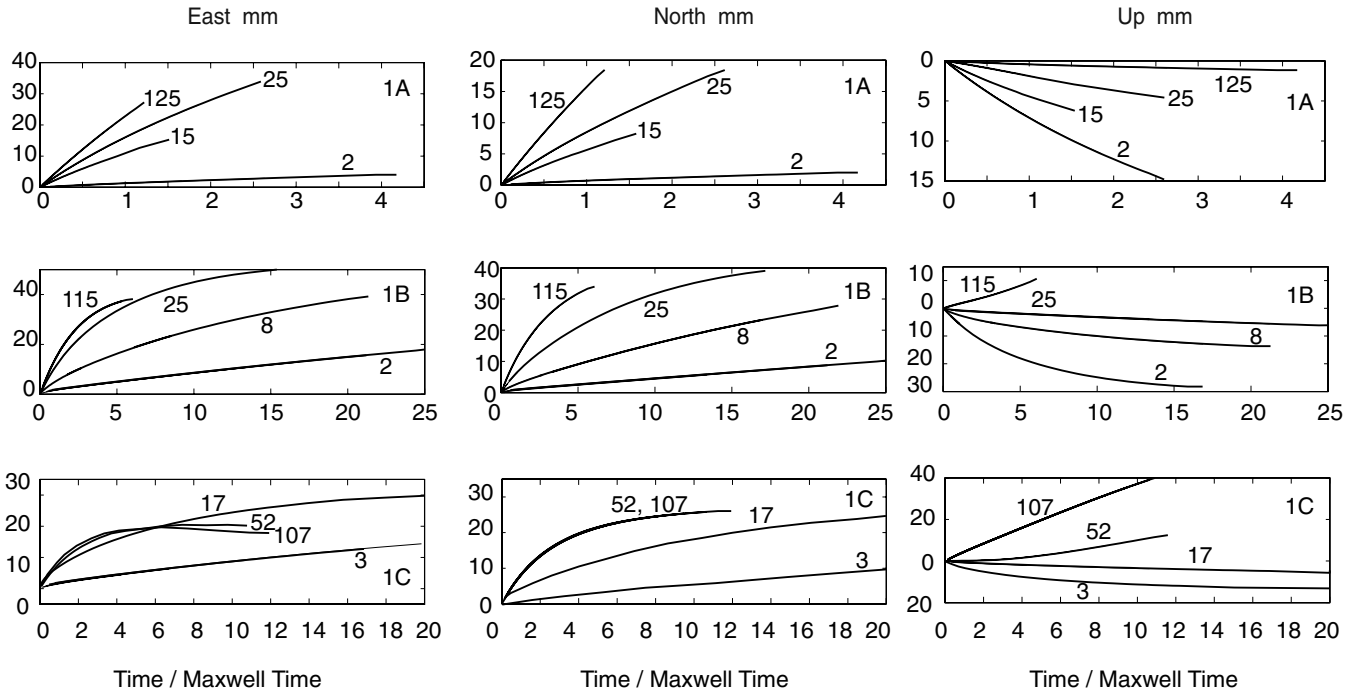

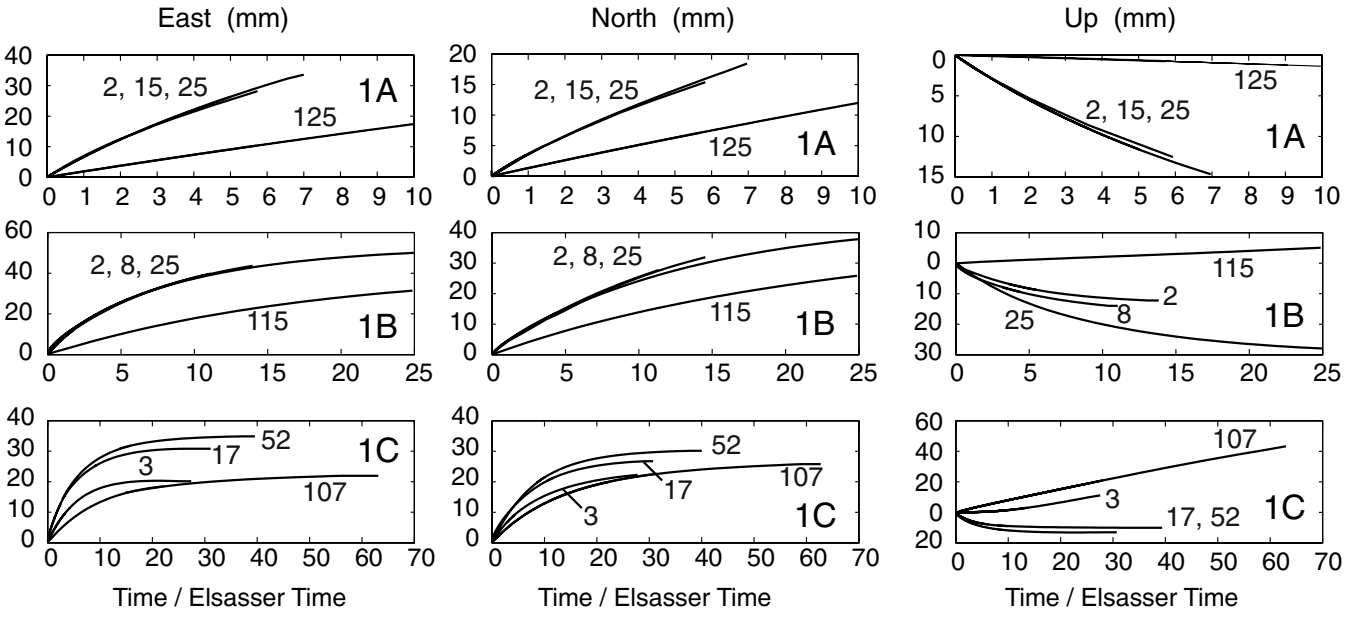

Figure A1. Displacement versus non-dimensionalized time (t/T_M and t/T_E) for group 1A, 1B and 1C models at hypothetical GPS sites D, E and F (locations shown in Figs 2 and 8). Different curve lengths on these plots arise from the fact that model simulations were run for 1 yr, rather than for a set number of Elsasser or Maxwell times. (Some models with longer Maxwell or Elsasser times were run for 7 yr.) Different time-dependent motion for the two horizontal components results in velocity azimuth changes during the early post-seismic interval. These figures supplement Fig. 11, and illustrate that distinct surface deformation may result from post-seismic relaxation of linearly viscoelastic crust or mantle layers, even for models with identical Elsasser times (T_E) and upper plate thicknesses (H).

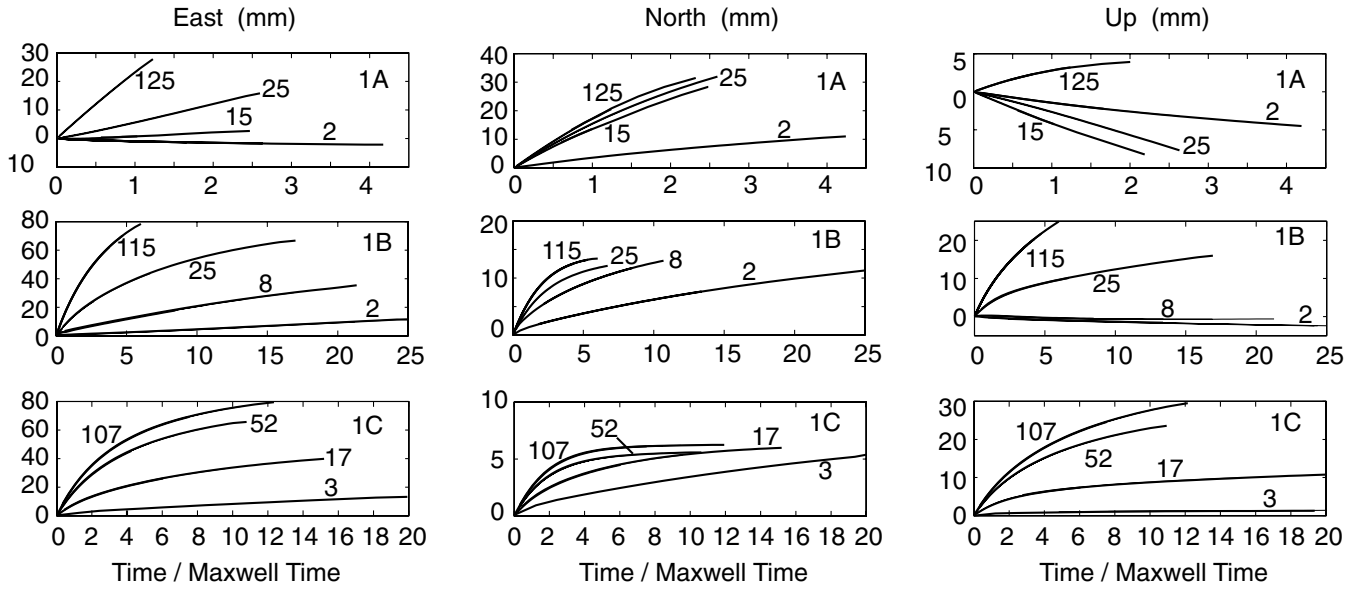

Appendix A: Station E displacements versus t/T_M

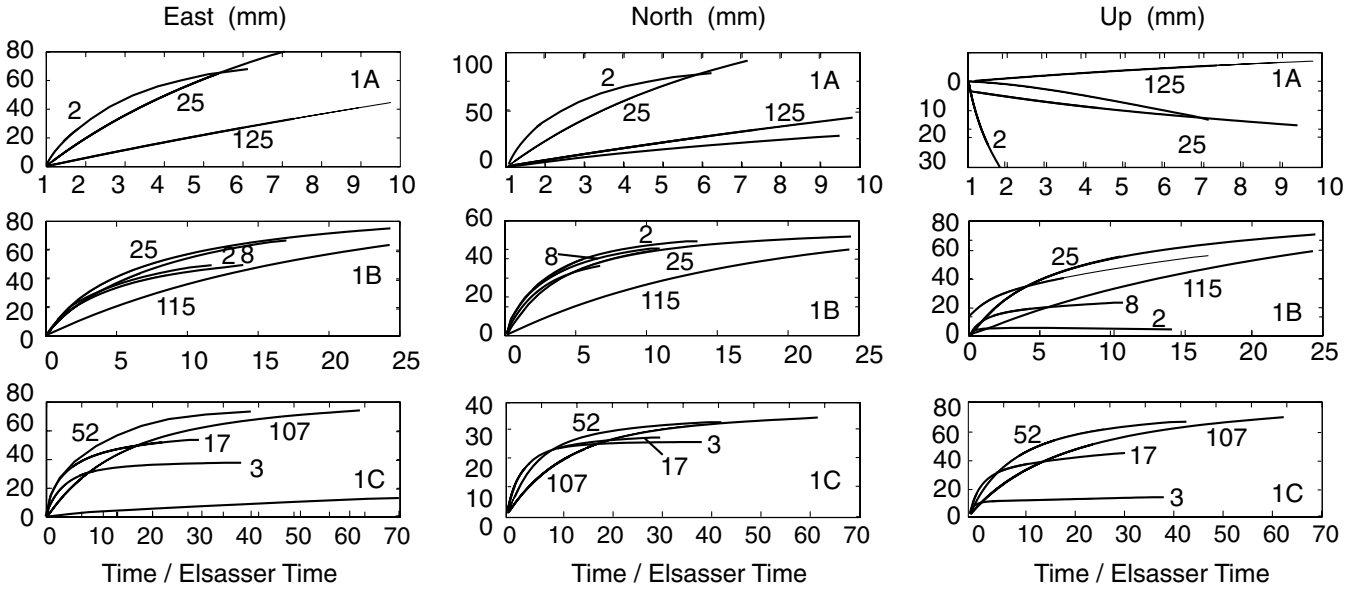

Appendix A: Station E Displacements versus t/T_E

Figure A1. (*Continued*.)

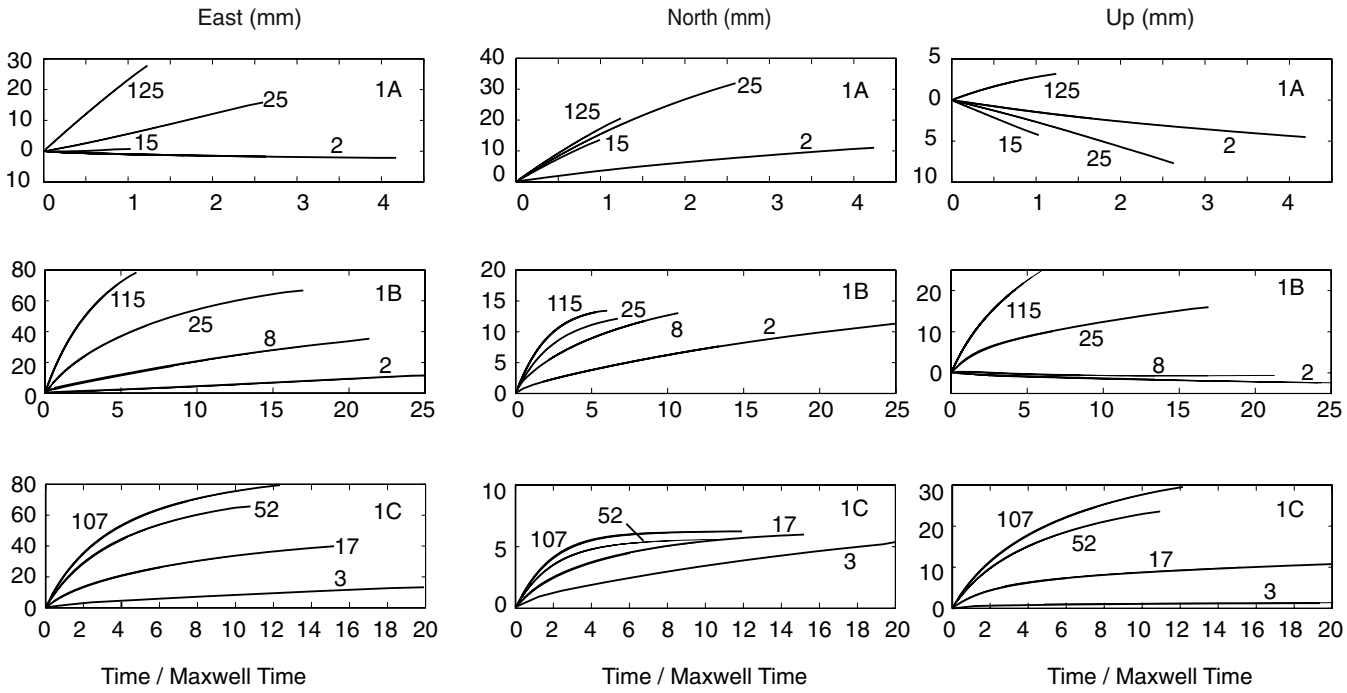

Appendix A: Station F displacements versus t/T_M

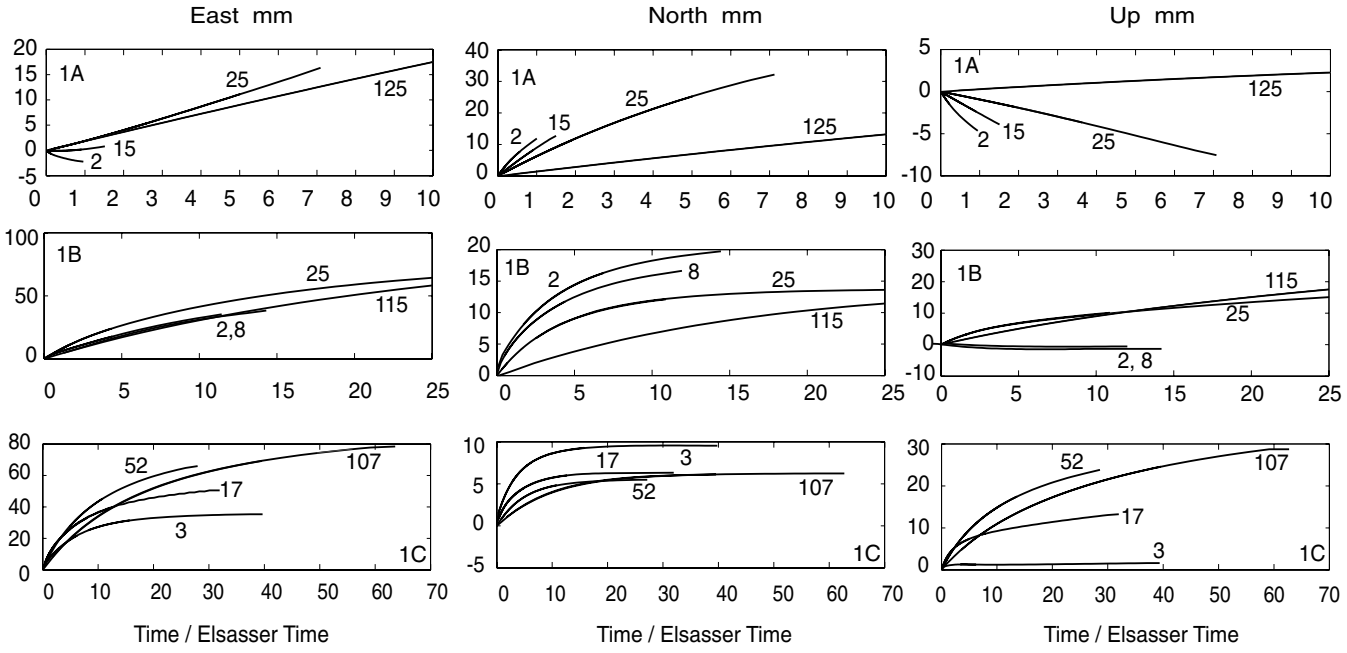

Appendix A: Station F displacements versus t/T_E

Figure A1. (*Continued*.)